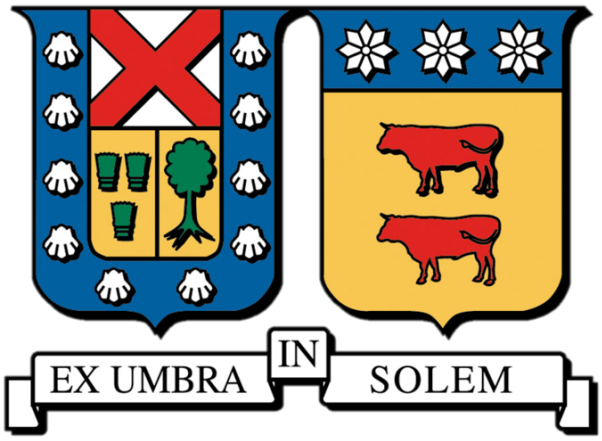
Hygromechanical properties of enzymatically-digested cotton based nanocellulose with modified wetting properties

Undergraduate Thesis for the degree of
"Bachelor of Science in Physics"
Departamento de Física, Universidad Técnica
Federico Santa María, Valparaíso, Chile, 2023.



Presented by Diego Jaramillo-Pinto.

ADVISOR : Dr. Tomas P. Corrales
COMMITTEE : Dr. Filipe Natalio
Dr. Ulrich Volkmann
Dr. Francisco Peña R.

"¿Dónde habrá una ciudad en la que alguien silve un tango?, ¿Dónde están los camiones de basura, mi vieja y el café?"

Luis Alberto Spinetta.

This thesis is dedicated to my family and pets.
Specially to Cofu and Gricel.

Acknowledgments

First, I would like to thank my family: My parents, René and Noelia, who had given me all I have ever needed since I was born, and have always trusted me. I could write a lot on how my childhood was in terms of studies, how my mom was always complaining with my teachers, how my dad was always at my side whenever I needed someone to take me into any place, but I can summarize it all in one phrase: I grew up happy. Thanks. My uncles-godparents and my grandfather. My cousin Carola, who lovely helped me to learn maths at school, and have always been like my older sister. Dani, nothing to say, you are my sun. Thanks for always teaching me how to live, without even trying to do it.

Now, I should say thanks to Prof. Dr. Tomas P. Corrales, for his guidance during this process. Prof. Tomas, you have taught me almost everything I know about research from zero. When I was a little pandemic-physicist that had never been in a laboratory, you trusted me to be part of your group, and embedded me with the art of experimental sciences. Prof. Filipe, you were the one who taught me how real science works, being always gentle, as well as tough. I will never forget how the first abstract that I ever tried to submit to a conference was trampled by you. Thanks for believing in me. Sebastián, you taught me everything you could about experiments and equipment development, while always being a nice lab company. I know that you will accomplish your dreams, and probably have a ship that travels through the ocean making beers. Do not forget to invite me sometimes. Thanks to Nicole Orellana, from Biotechnology, without you none of this could have been possible.

Thanks to my friends, that have supported me in every possible way. You are all amazing mates. Jorge, your notes on elastic deformations were extremely useful for this work. Carlos 2z, Líderes, good friends.

Tami, for the support, the affection, and the company throughout these years. For being always there and cheering me up whenever I needed. Thanks, love you.

My girlfriend Simona, you were my main support in the process of writing this document, providing me with the best coffee, love and happiness that I could have ever asked for. Thanks for being you, and for making this world happier.

This work was funded by ANID through project Fondecyt Regular 1211901 "Multiscale Mechanical Properties of Hygroscopic Nanofibers" and "Millennium Nucleus in NanoBioPhysics" project NNBP NCN2021_021.

Abstract

During the last decades, cellulose-based materials have rapidly gained importance due to their abundance and sustainability. By combining the growth of cotton in tissue culture with molecularly-designed glucose building-block feeding, cotton fibers with tailored properties can be obtained. The goal of this project is to study the hygromechanical properties of nanocellulose with modified wetting properties using environmental Atomic Force Microscopy (e-AFM).
Here we present a protocol to synthesize cotton fibers using enzymatic digestion based on cellulase, that yields nanofibrils. The enzymatically digested nanofibrils are then imaged using e-AFM, and their mechanical properties are measured under controlled relative humidity (RH) conditions.
Preliminary results evidence that unmodified cellulose samples increase their Young's modulus, while reducing their height with the decrease of rh. Meanwhile, modified samples are observed to be smaller than control ones, being more difficult to analyze mechanically.
Future experiments will focus on on comparing control samples with modified ones at different humidities.

Resumen

En las últimas décadas, materiales basados en celulosa han ganado importancia rápidamente, debido a su abundancia y sostenibilidad. Combinando el crecimiento de algodón en cultivo de tejidos con alimentación de bloques de glucosa diseñados molecularmente, fibras de algodón con propiedades adaptadas pueden ser obtenidas. La meta de este proyecto es estudiar las propiedades higromecánicas de nanocelulosa con propiedades de mojamiento modificadas usando Microscopía de Fuerza Atómica ambiental.
Se presenta un protocolo de síntesis de fibras de algodon para obtener nanofibras de celulosa, usando digestión enzimática basada en celulasa. Luego son presentados resultados en imágenes de las fibras y mediciones de sus propiedades mecánicas bajo humedad relativa controlada, usando el modelo de Hertz de la mecánica de contacto.
Los resultados muestran que la celulosa sin modificar se endurece y reduce su altura con la disminución de humedad relativa, además de que las fibras modificadas son más pequeñas que las de control, con lo que el análisis mecánico se dificulta. Experimentos futuros se enfocarán en hacer los mismos análisis realizados para las muestras de control en las modificadas.

Contents

Acknowledgments **iii**

Abstract **v**

1 Introduction **1**
1.1 Polymers . . . 7
1.1.1 Cellulose Polymer . . . 7
1.1.2 3-deoxy-3-fluoro-D-glucopyranose . . . 8

2 Measurement Fundamentals **11**
2.1 About Elastic Deformations . . . 11
2.1.1 Hertz Model of solids in contact . . . 15
2.2 Atomic Force Microscopy Fundamentals . . . 16
2.2.1 AFM Imaging . . . 18
2.2.2 AFM Force Spectroscopy . . . 20

3 Experimental Setups and Protocol **23**
3.1 Sample Synthesizing . . . 23
3.1.1 Synthesis equipment . . . 23
3.2 e-AFM setup . . . 25
3.2.1 Cantilevers used . . . 26
3.2.2 Anti-static Mat . . . 26

4 Results and Discussion **27**
4.1 Results . . . 27
4.1.1 First Phase . . . 27
4.1.2 Second Phase . . . 34
4.1.3 Final Discussions . . . 49

5 Conclusions and Outlook **51**

Bibliography **53**

Chapter 1

Introduction

Matter can be formed in different ways. This can sound obvious, since all the things that we see and know are matter, and usually look and feel very different. From the point of view of condensed matter physics, we can study how the fundamental structures of matter assemble with each other to form bigger structures, in particular, **mesoscale structures**, which will be of interest in this research work. One path that the atoms can follow is to bond together and form regular crystals. Studying this is how many solid state physics courses start[1], defining ***lattices*** as a set of points where the environment of any of those points is equivalent chemically to any other, i.e. regular and periodic structures. Another path is that the atoms bond together to form molecules, and those molecules interact with another ones by weak van der Waals bonds. That is a ***molecular crystal***. In liquids, atoms are attracted and form bonds, but they are not strong enough to be **permanent bonds**, even temperature could be high enough to make the bonds unstable. In liquids and gases, molecules of an array are free to move around into a new array.
The present research is mainly focused on Cellulose, which is a biopolymer with very interesting properties. It is not classified as crystalline, neither completely amorphous [2], and nowadays has many applications, specially for its sustainability and abundance. For example, in the textile industry [3]. Vast research efforts have been placed on **nanocellulose**, using very different methods to synthetize the polymers that are studied, while working with different sources. In the work of Chakraborty et al. [4], a general analysis on characterization techniques is done, making clear that Atomic Force Microscopy (AFM) analysis is an interesting technique to understand the properties of nanocellulose (Fig. 1.2). This work also concludes that AFM is able to provide better details of surfaces than Scanning Electron Microscopy (SEM) and yield mechanical/chemical properties of the sample, even validating some results that were obtained with Infrared Spectroscopy (IR).

[1] This topic is covered thoroughly in [1]

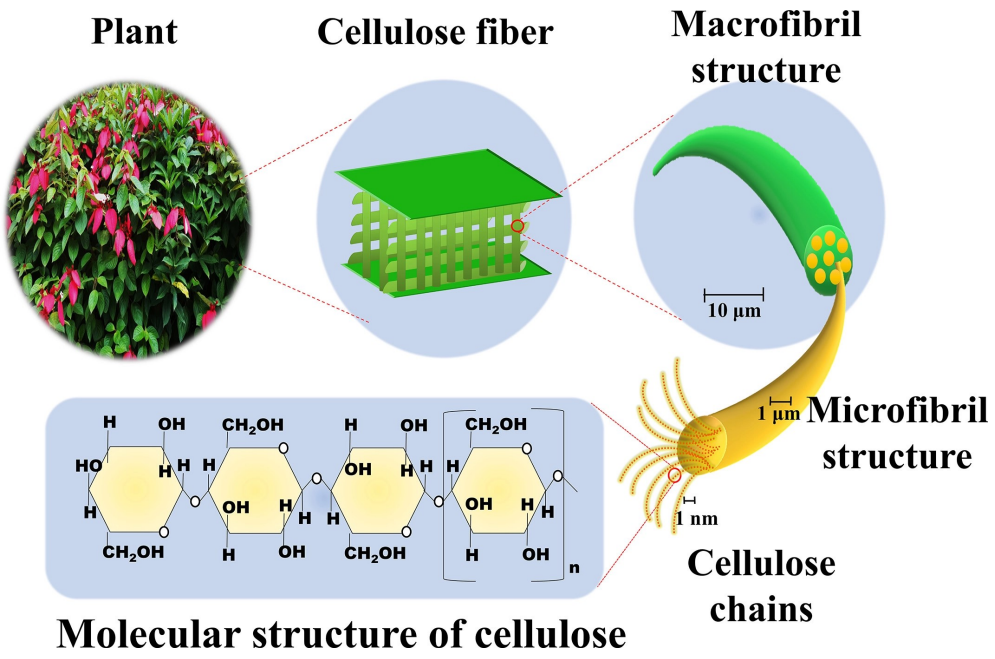


Figure 1.1: Plant-based Cellulose schematic structure. (Image taken from Chakraborty et al. [4]).

There have been successful methods to synthesize nanocellulose from different sources developed. For example, in the work of Fahma et al. [5], cellulose nanofibers (CNF) were obtained from **oil palm empty-fruit-bunches** by sulfuric acid hydrolysis (See Fig. 1.3). In that experiment, the average thickness of CNF was within 1-3.5[nm], and the degree of crystallization rounded 53.83% and 58.78% depending on the time of exposition to the sulfuric acid. CNF had cylindrical form. An interesting thing evidenced in this work is that, in the hydrolysis process, the acid generally has troubles penetrating the crystaline regions, so the amorphous region of cellulose is attacked first. This can be seen with X-Ray Diffraction (XRD), noting that when the cellulose was exposed to the sulfuric acid, it first increased its degree of crystallization, while as the time passed, it decreased. Another interesting work is that from Li et al. [6], where CNF synthesized via hydrolysis using sulfuric acid are shown, but this time they comes from **cotton**. The fibers had cylindrical form (rod like) and a smooth surface, with average lengths varying from 90.5[nm] to 664.9[nm], and widths varying from 7[nm] to 19.2[nm] (See Fig. 1.4). In this work, information regarding the crystallinity of nanocellulose from different sources was reviewed, showing variations from 54% to 87.1%. The crystallinity of CNF should also have something to do with the wetting properties of the cellulose [7].

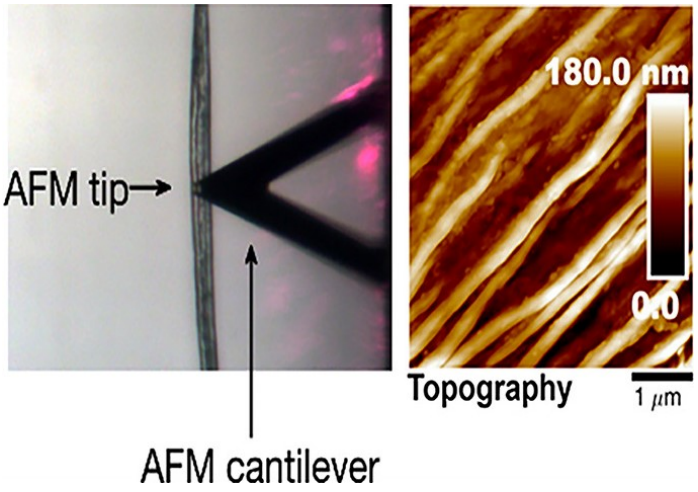


Figure 1.2: Left panel: Optical image of the AFM probe in contact with cotton fibers. Right panel: Topography map of a cotton based cellulose sample. (Image taken from Chakraborty et al. [4]).

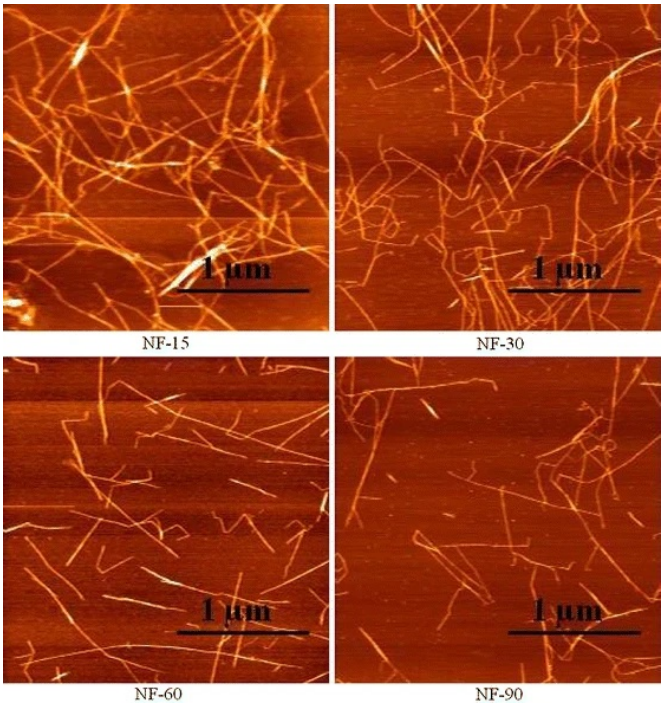


Figure 1.3: AFM images of CNF obtained from oil palm empty-fruit-bunches. The number after the dash on the code of the images refers to the time exposed to sulfuric acid, in minutes. (Image taken from Fahma et al. [5]).

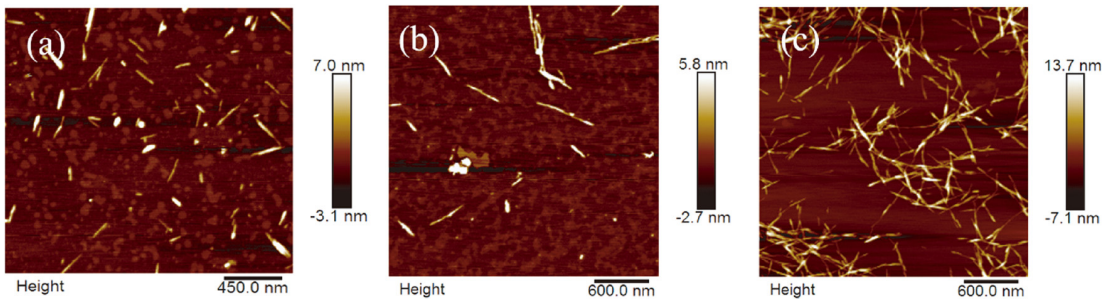


Figure 1.4: AFM images of cotton-based nanocellulose digested by sulfuric acid. Fibers with different times of exposition to sulfuric acid are shown (decreasing from left to right). Their lengths and width decrease with more time of exposition. Image taken from Li et al. [6].

The study of how materials and polymers respond to water is its own field of study. A research about CNF swelling was done by Ottesen and Syverud [7]. In particular, they studied how the Degree of Crystallinity (DoC) affects the swelling, and found interesting results (showin in Fig. 1.5). They concluded that there is a correlation between DoC and swelling. Higher DoC implies lower swelling. That evidence should imply that nanocellulose from different sources (with different DoC) would have different swelling properties.

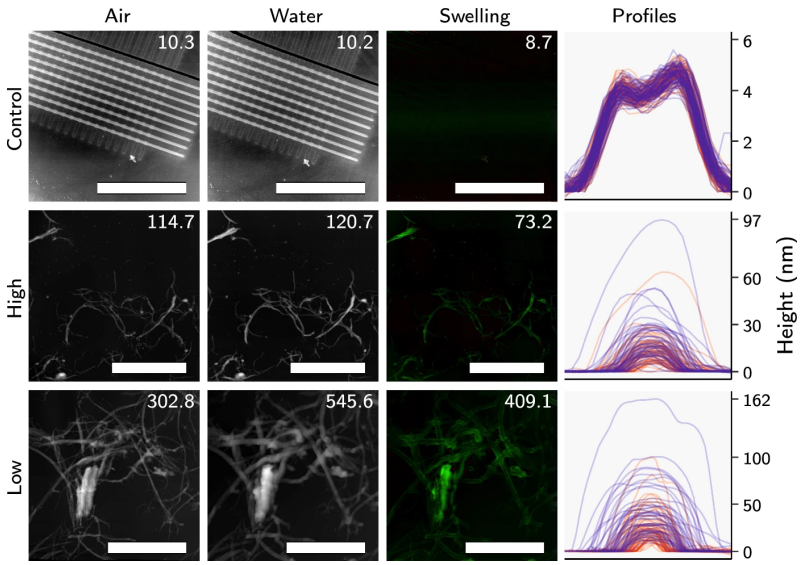


Figure 1.5: AFM micrographs of CNF with high DoC and low DoC in air or water as indicated. In the swelling column, the change in height. Scale bar is 5[μm]. Top right corner of the images indicates the max height registered. (Image taken from Ottesen and Syverud [7]).

In 2017, **biological** fabrication of cellulose fibers with **tailored properties** was achieved by Natalio et al. [3], where cellulose with magnetic and fluorescent properties were obtained. This was an important advancement towards improving the characteristics of cotton, thinking of it as a basis of smart textiles (adaptive materials that integrate multi-functionalities to dressing clothes [8], see Fig.1.6).

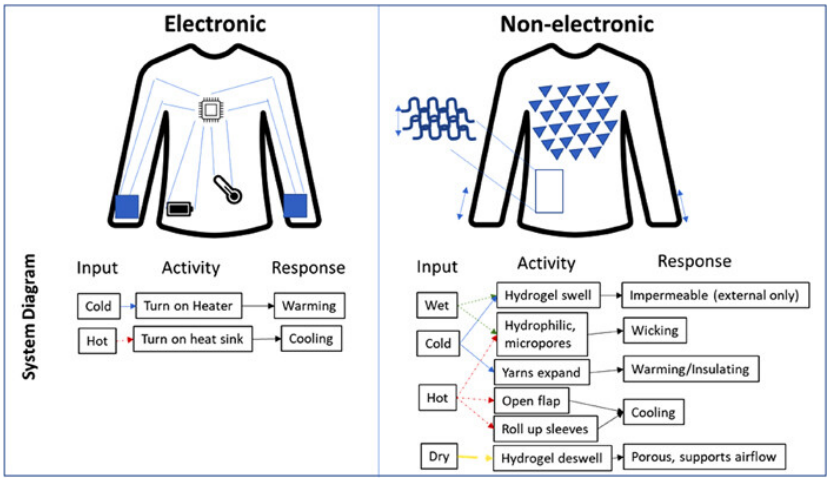


Figure 1.6: An example of what can be done with smart textiles in order to reduce problems of wearable clothes, using electronics. (Image taken from [8]).

In Fig. 1.7 we can see a scheme of the method used by Natalio et al. [3]. In summary, they combined *In vitro* cotton culture with molecularly designed glucose derivatives, obtaining unnatural properties from cotton fibers, such as magnetism and fluorescence. In plants, cellulose fibers are composed of β-glucopyranose units linked by the β-1,4-glycan bonds extruded as nanofibrils to the extracellular space of the plant ovule, where they self-assemble into larger micro to centimeter size structures through H-bonds. Natalio et al. [3] conclude that biological systems combined with appropriate molecular designs can be exploited in order to obtain functional composite materials, implementing the concept of **material-farming**.
Following the same line, the next step was to search for cotton with different modified properties, that could be more useful for the textile actual scenario. The new challenge became to obtain hydrophobic cellulose fibers, in order to get waterproof cotton clothes, without the need of any coating or chemical treatment, and that is the motivation of this research.

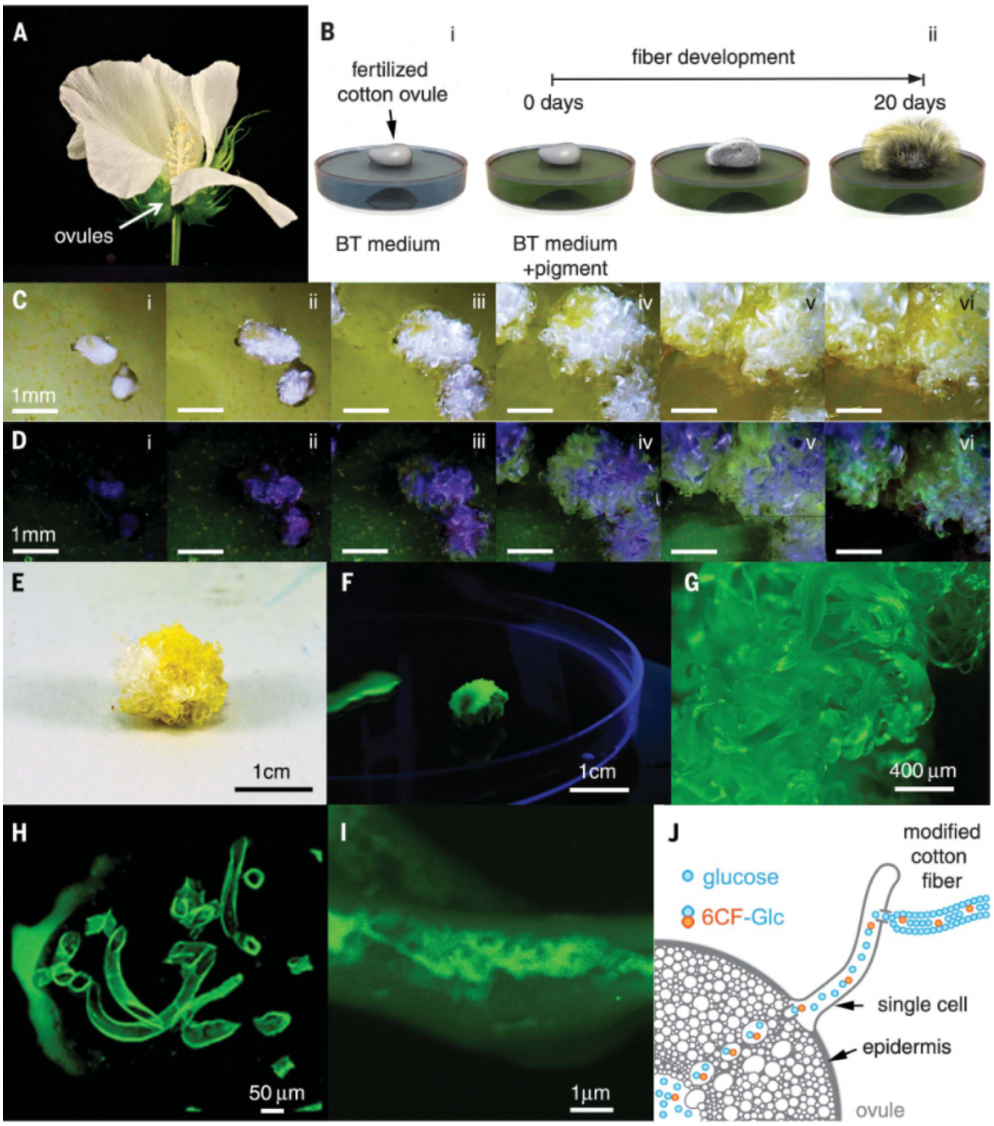


Figure 1.7: Schematic of the biological incorporation of fluorescent tagged glucose into cotton fibers. (Image taken from [3]).

In the remainder of this chapter, the theory of polymers, and more specifically of cellulose, will be discussed, in order to understand the work-material. We emphasize that the chemical detail of cotton modification is not the main focus of this thesis. Our goal is to study the morphology and mechanical properties of modified cotton, which is provided by our international collaborators.

1.1 Polymers

Also known as **macromolecule**, a Polymer is a set of N **molecular units** that are linked together by covalent bonds and form a chain. The molecular units (also known as chemical repeat units or monomers) can be all the same or can be different, but what defines a polymer is that modifying some quantity $n \ll N$ of monomers, does not affect its properties. Also, N is denoted as the **degree of polymerization**. One of the simplest polymers that we can synthesize is the polyethylene (PE), which as it name says, is a chain composed of N ethylene chemical units.

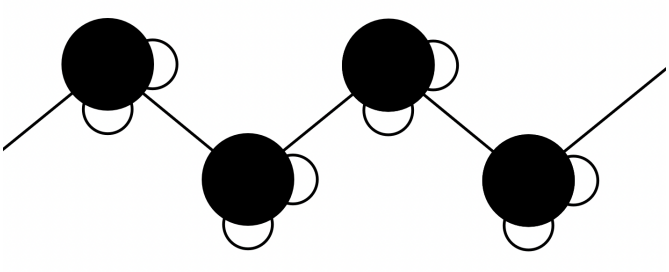


Figure 1.8: Polyethilene representation. Black and white spheres represent Carbon and Hydrogen respectively. Its chemical unit is CH_2.

Polymers in general have a similar structure to that of PE, usually being based on a Carbon back-bone, and replacing the Hydrogen atoms. It is important to know how a chain could be distributed in space in order to study it, since crystalline or amorphous forms can be presented. In order to understand and model polymers, various models, that will not be reviewed here, are developed. Many of them are covered in Strobl [9]. Another thing that is worth to notice in this work, is that a polymer can be either hydrophilic or hydrophobic (like or dislike water respectively), meaning that their response to environmental relative humidity will be determined by their internal capability to absorb water.

1.1.1 Cellulose Polymer

Celullase and Cellulose Breakdown (cellulolysis)

Cellulose is an organic polymer compound that can be found in nature and it is one of the most abundant polymers on earth [10]. The polymer chain of cellulose is composed of monosaccharide units (glucose hexose), i.e., it is a polysaccharide, which can be produced by plants and bacteria. In this work we will mainly focus on plant-based cellulose. The role of cellulose is fundamental for keeping the structure of the plant cell walls stable. It is, by default, hydrophilic, and water-insoluble [11]. The cellulose polymer can be represented as shown in Fig. 1.9.

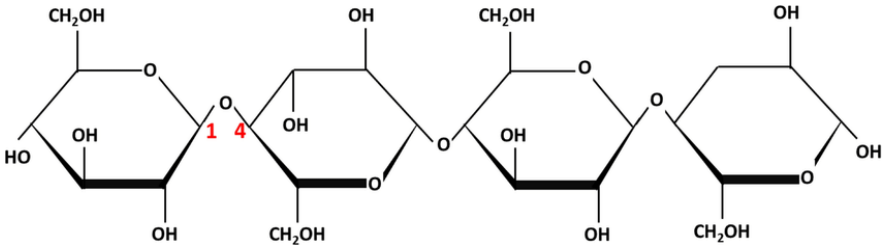


Figure 1.9: Cellulose polymer representation. (Image taken from [12]).

In order to study a cellulose-based macroscopic material, we must break them down to their fundamental building blocks. The process that will be of interest in this research is Cellulolysis Breakdown, which is a hydrolysis reaction that is produced by cellulase. Cellulase is an enzyme that hydrolyses cellulose, breaking its chemical bonds and isolating nanoscale components. Simply speaking, if one puts cellulose (cotton, for example) into a cellulase-water dilution, it should eventually break its bonds and generate isolated nanostructures. The protocol for doing this will be discussed in chapter 3.

1.1.2 3-deoxy-3-fluoro-D-glucopyranose

To obtain modified cotton samples as explained before, a mixture between glucopyranose and 3-deoxy-3-fluoro-D-glucopyranose (3dfg) is fed to the cotton plant ovule. Notice that 3dfg is a molecule that, in simple words, is a glucopyranose with its -OH group from Carbon-3 replaced with a Fluorine (See Fig. 1.10). The idea is that the cotton ovule is not able to distinguish between glucose and a mixture of glucose with 3dfg molecules. The fluorine atom that 3dfg has, should modify the wetting properties of the final cellulose that composes the cotton.

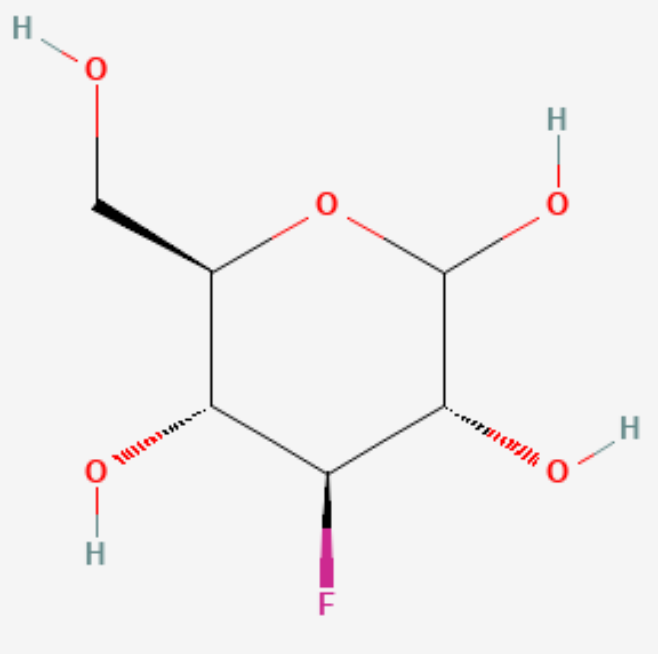


Figure 1.10: 3-deoxy-3-fluoro-D-glucopyranose molecule representation. (Image taken from [13]).

The treated cellulose fibers analysed in this work, presented in chapter 4, were extruded from cotton cultivated *in vitro*, fed with compounds of glucose and 3dfg.

In this thesis, we aim to study the hygromechanical properties of enzymatically-digested cotton based nanocellulose with modified wetting properties, using environmental Atomic Force Microscopy (e-AFM). Note that the concept of **hygromechanics** refers to the mechanical properties with a variable controlled relative humidity (As can be found in the work of Zhang et al. [14]). In chapter 2, the theory behind AFM will be introduced, while chapter 3 will focus on experimental setup and protocols. Within chapters 4 and 5, the results and conclusions will be presented, respectively.

Chapter 2

Measurement Fundamentals

In this chapter, a brief review on elastic deformations will be shown to introduce the Hertz Model, which will be used to compute the Young's Modulus of the nanofibers analyzed with e-AFM in chapter 4. Then, the fundamentals of AFM will be introduced, and the requirement of supersharp-tips in our experiment will be discussed.

2.1 About Elastic Deformations

The approach taken in this section to introduce deformation theory is extensively covered in the books of Taylor [15] and Landau et al. [16]. As preliminary definitions, we can consider the following:

- Surface force: A force that acts perpendicularly to a surface, and increases proportionally to its area. Any surface force can be decomposed in terms of Tension, Pressure, and Shear forces.
- Tension force: Any force that acts in the same orientation as the normal vector to a surface.
- Pressure force: Any force that acts in the opposite orientation as the normal vector to a surface.
- Shear force: Any force that acts parallel to a surface.

Representation of these type of forces is presented in Fig. 2.1. As forces acts all over a given area, it is natural to define relations between both quantities. That is what will be covered next.

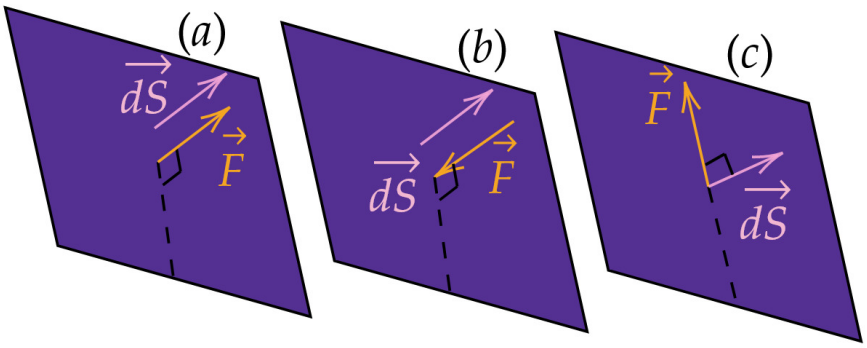


Figure 2.1: Representations of (a): Tension Force, (b): Pressure Force, (c): Shear Force, acting onto a surface. $\vec{dS}$ represents the area vector, normal to the surface, while $\vec{F}$ represents the applied force vector.

Stress

Stress (σ) is defined as the ratio between the force applied and the area of application:

$$d\sigma := \frac{d|\vec{F}|}{dA}. \tag{2.1}$$

The differential form appears in order to consider any surface, having curvature or not. Of course, in a uniform surface, stress can be stated as:

$$\sigma = \frac{|\vec{F}|}{A}, \tag{2.2}$$

which is the definition used for pressure in a static fluid, for example. Note that as it is defined with the magnitude of the force, it can count with tension, pressure, or shear forces. Furthermore, it can be decomposed in components of every of them. The stress usually results in a deformation of the body in which it acts, and that deformation can be quantified in terms of the original body, i.e., strain.

Strain

Strain (ϵ) is defined as the ratio between the deformation of a geometric characteristic of the body, and its initial state (usually equilibrium). This characteristic could be volume, length, and others. The easiest way to see the concept is thinking in length, as presented in Fig. 2.2 and Fig. 2.3. A deformation was made if the distances between points of the body changes. In both example presented, one of the particles started in point B and ended at point C.

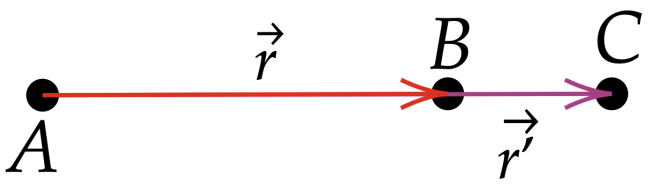


Figure 2.2: Representation of a longitudinal deformation caused by a tension stress. Initially, there was a particle in B, then it moved to C.

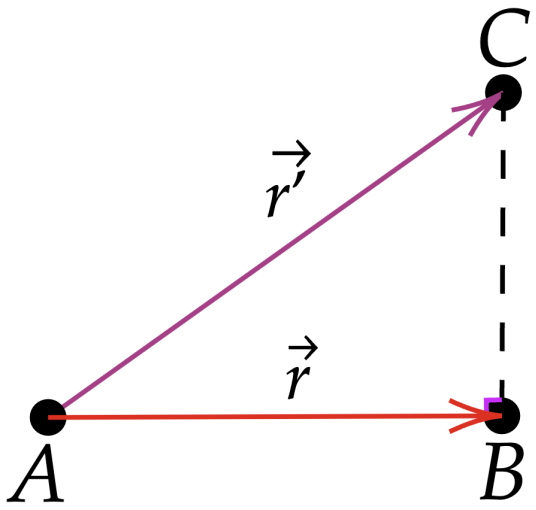


Figure 2.3: Representation of a shear deformation caused by a shear stress. Initially, there was a particle in B, then it moved to C.

The distance vector between A and B changed from $\vec{r}$ to $\vec{r'}$ in both cases, so strain can be defined as:

$$\epsilon := \frac{|\vec{r} - \vec{r'}|}{|\vec{r}|} = \frac{|\vec{\Delta r}|}{|\vec{r}|}. \tag{2.3}$$

Note that Fig. 2.2 shows a scaling of the original length, so we could write $\vec{r'} = \alpha\vec{r}$. If $\alpha > 0$, the length increases and it must be caused by a tension stress. If $\alpha < 0$, a tension stress is being applied, and so the length decreases. Fig. 2.2 shows the case with $\alpha > 0$, but the concept still runs for both cases. In the case of shear strain presented in Fig. 2.3, as $\vec{\Delta r}$ is orthogonal to $\vec{r}$, $\epsilon = \tan\theta$, with θ the angle between $\vec{r}$ and $\vec{r'}$.

Young's Modulus

Lets consider two points of a body separated by a distance dx. In the case of small deformations, we know that materials should follow the Hooke's law, then, it can be written:

$$d\vec{F}_{rest} = -kd\vec{u}, \tag{2.4}$$

where $\vec{F}_{rest}$ corresponds to the restoring force, $\vec{u}$ to the deformation vector, and k to the elastic constant of the material. Thus:

$$d\vec{F}_{ext} = -d\vec{F}_{rest} = kd\vec{u}. \tag{2.5}$$

Writing the displacement in terms of stress and strain following Eqs.(2.1),(2.3):

$$dF_{ext} = kdu \Rightarrow \sigma dA = k\epsilon dx \Rightarrow \sigma = \epsilon \underbrace{\left(\frac{dx}{dA}k\right)}_{E}. \tag{2.6}$$

The step realized in Eq.(2.6) was made considering that the Eqs.(2.1),(2.3) allow to stablish the relation $du = \epsilon dx$ and $dF = \sigma dA$. From Eq.(2.6), the quantity named as Young's modulus (E) appears. The Young's modulus depends only on the properties of the material, and it makes account of the linear stiffness that a material has. There exists the equivalent for shear forces (Shear modulus, G), but that will be of no interest for this research.
In order to compute the Young's modulus of a material from which we do not know any of the terms that are shown in Eq.(2.6), different models are used. The simplest one, and the one that will be used on this work is the Hertz Model (Sec. 2.1.1).

2.1.1 Hertz Model of solids in contact

In this section, some important results, as well as the considerations took by the Hertz Model will be briefly presented. The work of Hertz [17] considered two spheres in contact, as represented in Fig. 2.4. Note that Fig. 2.4b. accounts of a flat circular contact surface, with radius a.

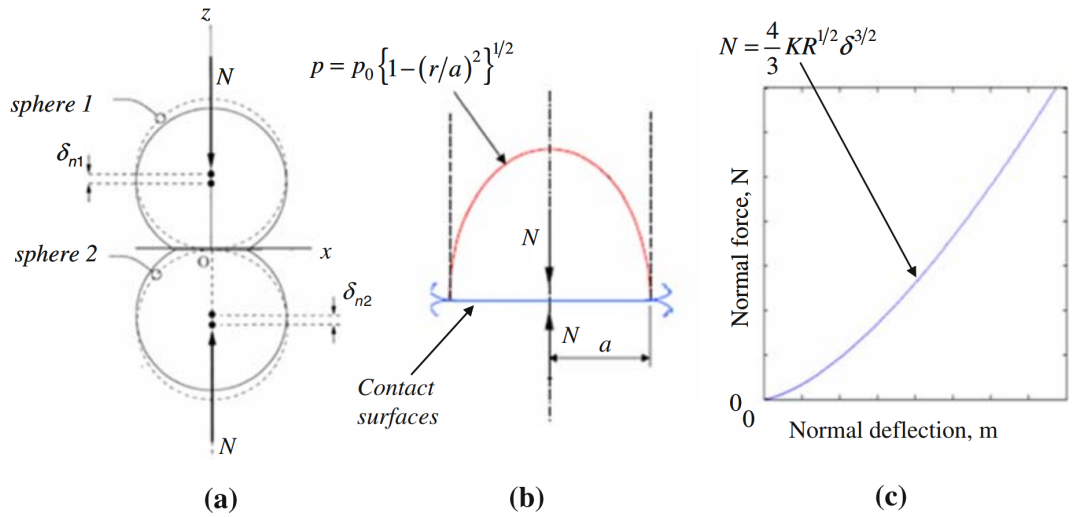


Figure 2.4: a) Action of the normal force (N), normal deflection (δ) and resulting contact surface. b) Contact pressure profile between the spheres. c) Typical normal force vs normal deflection curve. (Image taken from [18]).

Following Hertz (and the analysis made in the work of Dintwa et al. [18]), the maximum pressure is given at the centre of the contact surface, $r = 0$, and is given by:

$$p_0 = \frac{3F}{2\pi a^2}, \tag{2.7}$$

where F refers to the applied force, that was named as N in Fig. 2.4. a can be written in terms of the effective stiffness (K) and the effective radius of curvature (R) as:

$$a = \left(\frac{3FR}{4K}\right)^{1/3}. \tag{2.8}$$

The definitions of R and K are the following:

$$\frac{1}{K} = \frac{1-\nu_1^2}{E_1} + \frac{1-\nu_2^2}{E_2}, \tag{2.9}$$

$$\frac{1}{R} = \frac{1}{R_1} + \frac{1}{R_2}, \tag{2.10}$$

where ν_i and R_i are the Poisson's ratios and radii of curvatures of both spheres. Finally, the normal deflection will be given by:

$$\delta = \left(\frac{9F^2}{16RK^2} \right)^{1/3}. \tag{2.11}$$

In case that one of the materials is much harder than the other one, having a Young's modulus of E, one of the terms of Eq. 2.9 would dissapear, yielding:

$$\delta = \left(\frac{9F^2E^2}{16R(1-\nu^2)} \right)^{1/3}. \tag{2.12}$$

For this model to be theoretically developed, many assumptions were taken into account [18]: 1) Materials of contacting bodies should be isotropic and homogeneous. 2) Static loads applied. 3) Dimensions of the bodies are much larger than contact radius. 4) Materials are Hookean (linearly elastic). 5) No friction effects are considered. 6) Small deformations. 7) Static loads are applied.
In reality, many of these assumptions cannot be applied. Nevertheless, the work of Dintwa et al. [18] showed that some of these conditions are not mandatory to be satisfied in order to get correct results using the model.

2.2 Atomic Force Microscopy Fundamentals

Atomic Force Microscopy (AFM) is a type of Scanning Probe Microscopy (SPM), invented by the 1980's, after the Scanning Tunneling Microscopy (STM) and Scanning Near-Field Optical Microscopy (SNOM). AFM has its own branches, such as Magnetic Force Microscopy [19] (a magnetized tip scans a magnetic sample) and Kelvin Probe Force Microscopy [20] (measures contact potential differences). An important difference between AFM and its predecessors is that it allows imaging topography of **conducting and isolating surfaces**, with atomic resolution [21]. Atomic resolution with AFM has been proven to be obtainable in vacuum, and even at room temperature [22].
The basic components of AFM (see Fig. 2.5) are a Laser, Tip, Cantilever, Piezo actuators and Photodiode (PD). The tip is the component that will interact with the sample, and is attached to a cantilever, generally made of silicon. The cantilever is used to measure the interaction between the tip and the surface, through the signal that PD receives from the laser, which is focused on the backside of the lever. The laser points the cantilever, and is deflected and caught by the PD, which typically has 4 quadrants (photosensitive regions). PD generates a current proportional to the photons caught in every quadrant. The Piezo actuators are piezo electric scanners that move the cantilever across the surface, and control the tip-sample distance.

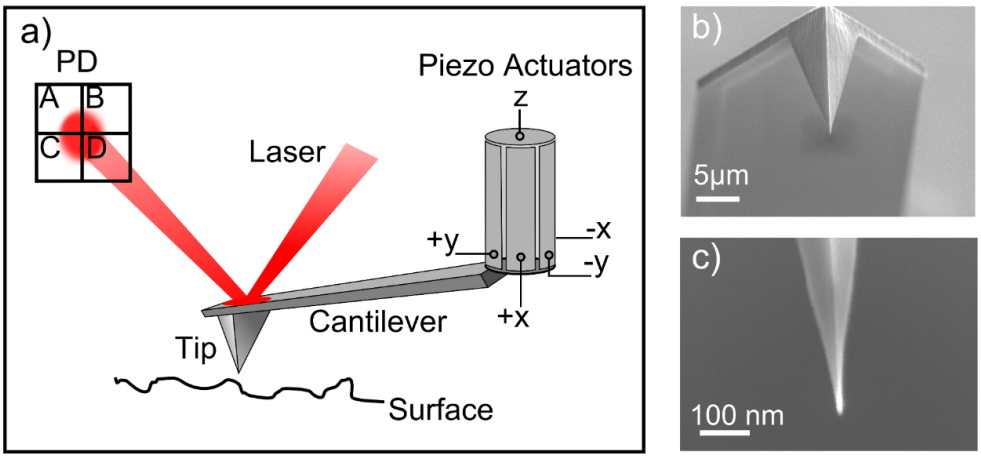


Figure 2.5: a) Basic AFM components representation. b) SEM image of a commercial cantilever with its tip. c) Zoom of a cantilever tip. (Image taken from Corrales [23]).

AFM topographical images are generated considering the tip-sample interaction, which is a mix of short and long range forces, that can be understood with a Lennard-Jones potential (see Fig. 2.6).

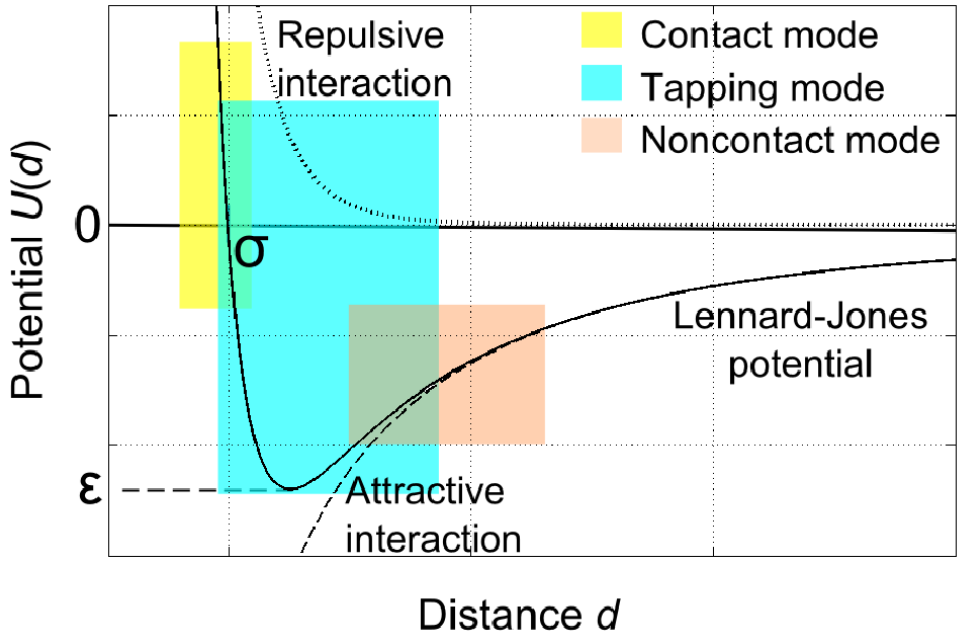


Figure 2.6: Representation of tip-sample interaction as Lennard-Jones potential, in terms of distance. The distances marked correspond to different AFM modes. (Image taken from [24]).

2.2.1 AFM Imaging

There are three principal modes for the AFM to operate doing images (Fig.2.8 shows an schematic of imaging in general):

- Contact mode: Cantilever-sample distance is less than a few Angstroms. The probe scans keeping a constant tip-sample force, considering that the interaction will be repulsive, thus being able to do a 3D topographical map [24]. From this mode, the Force spectroscopy that will be presented later was developed.

- Tapping mode: The cantilever vibrates near its mechanical resonance frequency (but not exactly at it). The resonance frequency is obtained doing a frequency sweep, using and additional piezo-actuator located on the cantilever holder. Once approached to the sample, the tip will *tap* or briefly touch the surface, reducing the vibration amplitude [25]. By taking the variation between the free-vibration amplitude and the vibrating amplitude that the tip has in every point as a setpoint, a topographical map of the surface can be done. This mode is also known as Amplitude Modulation (AM) mode.

- Non-contact mode: The cantilever vibrates near its resonance frequency. As the tip approaches close enough to interact with the sample, the force between them would be enough to produce a shift in the frequency from the resonance one. The change in frequency is related proportionally to the gradient of the interaction force. To see this, we start considering the frequency of an interacting cantilever and then doing the considerations shown in [23]:

$$f = \frac{1}{2\pi}\sqrt{\frac{k*}{m}} \tag{2.13}$$

$$= f_0 + \frac{1}{4\pi m}\sqrt{\frac{m}{k_0}}k* \tag{2.14}$$

$$\Rightarrow \frac{\Delta f}{f_0} = \frac{1}{2}\frac{k*}{k_0} = -\frac{1}{2k_0}\frac{dF}{dz}. \tag{2.15}$$

  f_0 is the non-interacting frequency of the lever, $k*$ the effective spring constant, and k_0 the lever's spring constant. By taking the shift in frequency as a setpoint, a topographical image is created. This mode is also known as Frequency Modulation (FM) mode.

The reason for using different modes is that they are optimized for different working. Contact mode have the advantage, for example, that it can measure lateral forces on a sample, but at the same time the disadvantage that the same movement can damage the tip or the sample. In the work of Zhong et al. [26], they

show differences between contact mode AFM and Tapping mode, in a polymer surface, concluding that tapping mode was way better at imaging (see Fig. 2.7), as it generated images without damaging the tip nor the sample, while contact mode induced irreversible damage in the polymer.

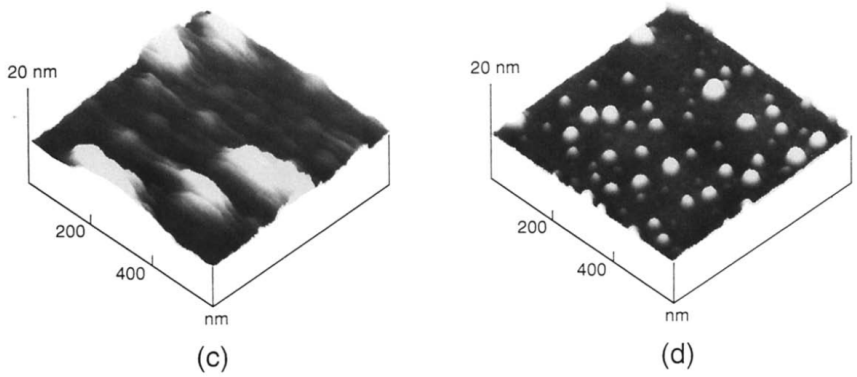


Figure 2.7: Comparison of AFM (c) Contact mode, (d) Tapping mode imaging on a Fractured polymer/silica fiber surface. (Image taken from [26]).

If the sample, and/or its topography, are very small (compared to the tip radius, which is commonly in the order of nanometers), the image generated can be disturbed from reality, since the tip would be hitting them for a longer period (See Fig. 2.9). This is a problem than can be solved generally decreasing the tip radius as much as it is needed. We will see the effect of this in chapter 4.

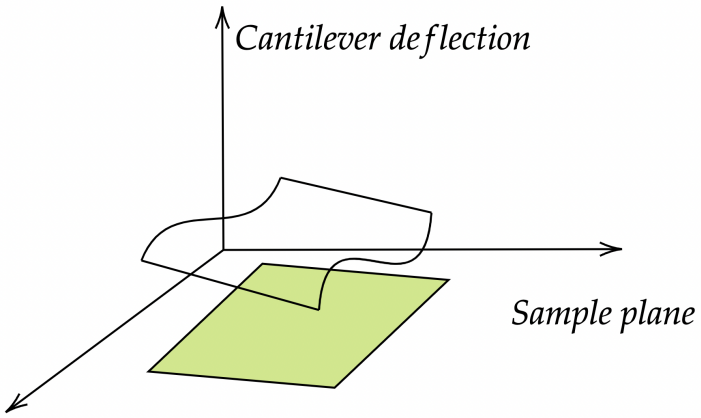


Figure 2.8: Schematic of how the topographical images are made. In the sample plane, only non-topographical components are considered.

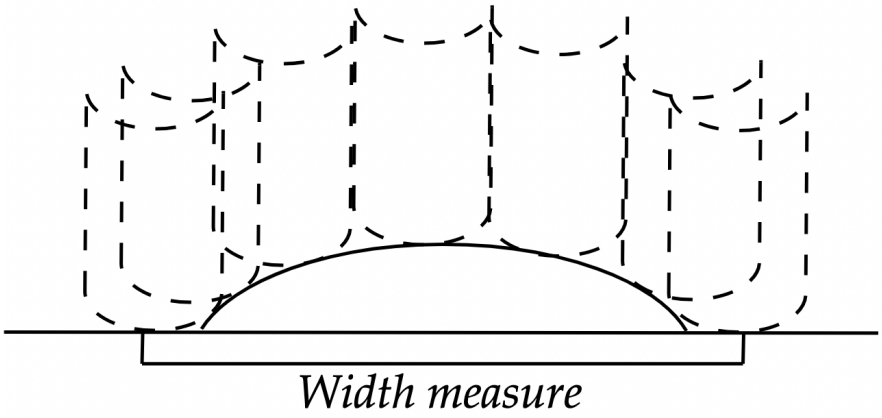


Figure 2.9: Graphical representation of how the dimensions of a sample measured with AFM can disturb the real topography if the tip radius is comparable to the sample scale.

2.2.2 AFM Force Spectroscopy

The Force Spectroscopy experiment consists on approaching the AFM tip onto a single point of the sample's surface in order to deform it, while its vertical position is measured by the Photodiode [23]. The movement is made by the Z-piezo actuator. In the moment that tip and sample are in contact, their deformation is understood as the one of two Hookean bodies (if the sample is deformable). This assumption is made under the understanding that the deformation should be small enough compared to the sample's total dimensions, so it can be considered an elastic deformation and not pass to the plastic regime. Then, the deformation of the sample (δ_s) in terms of total deformation (δ) and the cantilever's deformation (δ_c). Knowing the cantilever's deformation and its spring constant (usually obtained from thermal noise method, as explained in the work of Hutter and Bechhoefer [27]) the deflection signal can be converted into applied force.
To measure a soft sample, a reference on a hard sample is taken. This allows to calibrate the deflection of the cantilever in terms of voltage, since the hard sample would not be deflected. Once the reference is done, a Force graph in terms of tip-sample distance can be made. This is shown in Fig. 2.10, where also approach-retract curves are shown. The approach retract curves in general are almost equals on hard samples.

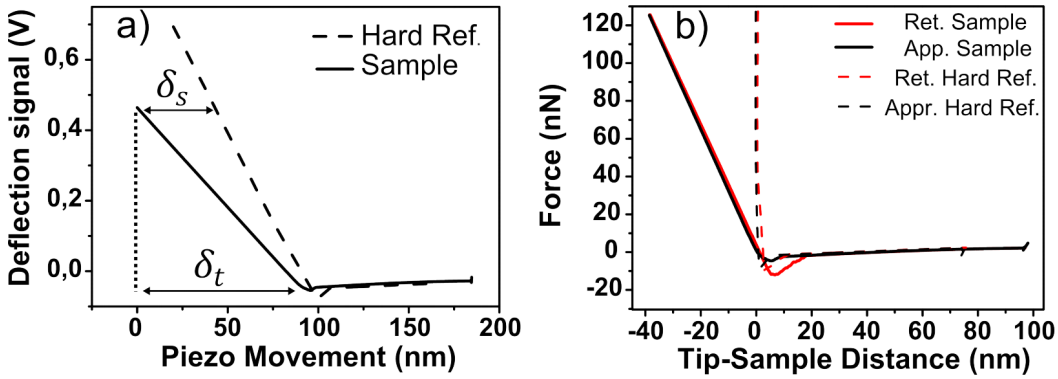


Figure 2.10: a) Reference curves, used to calibrate the microscope's sensitivity. Hard and soft samples are illustrated. b) Final converted Force curves in terms of tip sample distance. Imagen taken from Corrales [23].

Fig. 2.10 shows another interesting phenomena that usually occurs on deformable samples, the hystheresis. Hystheresis of the approach-retraction curve can be caused by factors, such as capillarity of the sample (dependent on the surface tension), sliding the tip on the surface, and others.

Chapter 3

Experimental Setups and Protocol

In this chapter, the synthesis protocol will be described, as well as the e-AFM setup. Additionaly, tools and equipment used for the synthesis and AFM analysis will be presented. Samples were sent by our collaborator, Dr. Filipe Natalio.

3.1 Sample Synthesizing

We take a cotton sample of around 10[mg] and dilute it on a cellulase-water 1.8$[g/L]$ dilution, in order to be digested. The cotton samples were grown in soil and in a greenhouse at the Weizmann Institute of Science greenhouse facilities. Cellulase is from *Trichoderma reesei*. The solution is left overnight for around 16 hours inside a thermoblock at constant temperature of 25°C without agitation. After the digestion is done, we take a 10$[\mu L]$ sample from the solution and dilute it 1:500 in water, followed by a mixing using Vortex. The stock sample is kept at 4°C until further experiments. Once mixed, we take 10$[\mu L]$ of the solution and dispose them into a silicon wafer, that was cleaned using isopropyl alcohol, generating a little drop on the surface. The silicon is put inside an incubator with a fixed temperature of 25°C in order to dry the drop, for 5 hours. The steps can be iterated to get more days of digestion, using the stock sample. Once the drop is completely dried, the sample is ready to be analyzed with e-AFM.

3.1.1 Synthesis equipment

The synthesis was made using equipment from the USM's department of Biotechnology. The steps required a Microbalance in order to weight the cotton sample, a Laminar Flow to make the dilutions, a Vortex Mixer to mix the dilution, a Thermoblock to maintain it at the desired temperature, and an incubator to dry the silicon's drop. The equipment in shown in Figs. 3.1 and 3.2.

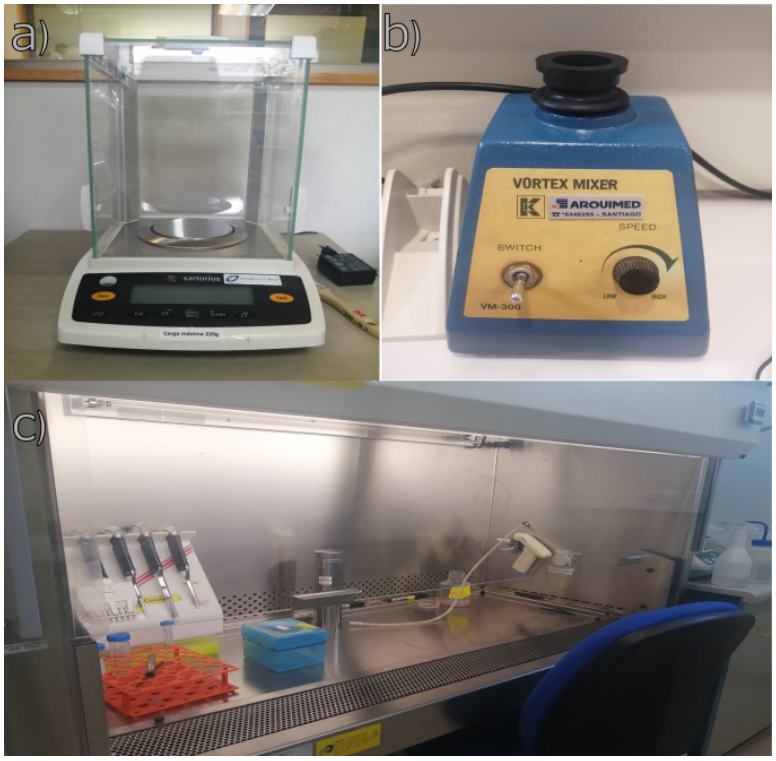


Figure 3.1: a) Microbalance, with a precision of 0.1$[mg]$. b) Vortex Mixer. c) Laminar Flow.



Figure 3.2: a) Thermoblock. b) Incubator.

3.2 e-AFM setup

The AFM we used in this work is a NanoSurf Flex AFM C3000, mounted with a humidity chamber (HC). HC is connected to little hoses that transport a flow of gas, which is a mixture of two entries. The first one comes from a bottle where a mixture of distilled water, air and nitrogen (99.998% purity, from INDURA) is done, with the help of a diffuser stone to create bubbles. The second one is a line of pure nitrogen, which can be used to dry the environment. Also, there is an exit hose, that allows to control the pressure on the HC. The range of humidities can sweep from around 2% and 65%. Additionally, a BME280 sensor, controlled by Arduino is on the floor of the HC. BME280 sensor has been proven to be a good option to measure temperature, pressure and humidity of different environments [28], being a low cost option to consider in order to even monitoring the quality of air in cities like Santiago, Chile [29].

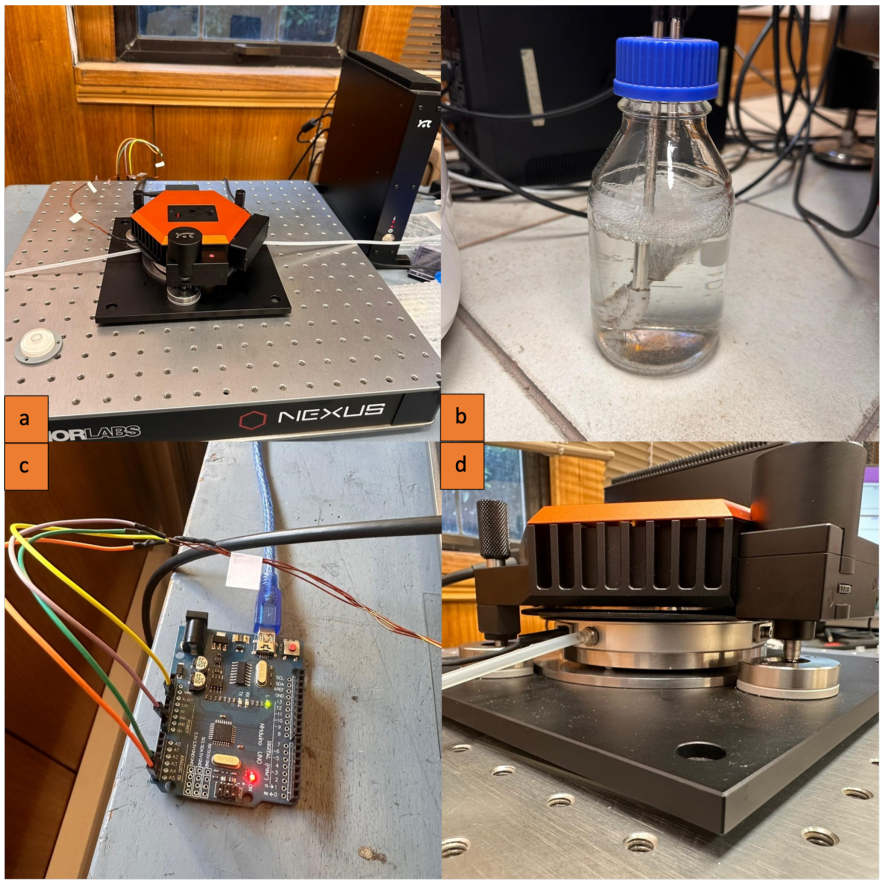


Figure 3.3: a) Flex AFM C3000. b) Bottle used to generate the gas that enters to the humidity chamber. c) Arduino connection used to measure the humidity sensor. d) Lateral photography of the e-AFM with the humidity chamber mounted.

3.2.1 Cantilevers used

The cantilevers used for this research were: **PPP-Zeihr** cantilever, with a tip radius and force constant of around 7[nm] and 27[N/m] respectively; **PPP-FMR** cantilever, with a tip radius and force constant of around 7[nm] and 2.8[N/m] respectively; and Supersharp **SSS-FMR** cantilever, with a tip radius and force constant of around 2[nm] and 2.8[N/m] respectively. It was measured by us that SSS-FMR used usually have force constants that range between 1.3-2[N/m].

3.2.2 Anti-static Mat

An Anti-static mat is used to mount the AFM probes, specially the SSS-FMR cantilever, since a small quantity of static electricity can damage the tip if discharged. It is highly recommended by the supplier of the Supersharp tips. In Fig. 3.4, we can see the bracelet that's needed to be put on ones' wrist, in order to increase own's resistance. The resistance measured with a Multimeter shows a value around 1.9 [MΩ].



Figure 3.4: Anti-static mat from NanoAndMore, used to mount the supersharp cantilevers.

Chapter 4

Results and Discussion

In this chapter, the results obtained from AFM experiments will be presented (Sec. 4.1). Additionally, in Sec. 4.1.3 these results shall be generally discussed.

4.1 Results

This section will be divided in two parts, called first and second phase. The first phase is an early stage of the work, where only control samples without using humidity chamber were analyzed. The protocol was not completely developed, so the dilutions were made differently. It will be presented mostly with the purpose of noticing how the course of this investigation developed, and how is experimentally evidenced the need of sharp-tips and protocol refinement. In the second phase, the protocol presented in Chapter 3 was applied. Also, control and 3-dfg samples were analyzed, using the humidity chamber to control RH.

4.1.1 First Phase

Two dissolutions were created following the protocol described in Chapter 3, but with the fourth stage changed to 1:100 dilution in water instead of 1:500. This leads us to samples with proportions of 1:100 and 1:200, which we will call dilution 1 and dilution 2 respectively. This stage of the process was characterized by the usage of the three cantilevers presented in Chapter 3. The difference between the three of them is noticeable, as will be discussed below.

Zeihr Cantilever (Day 1)

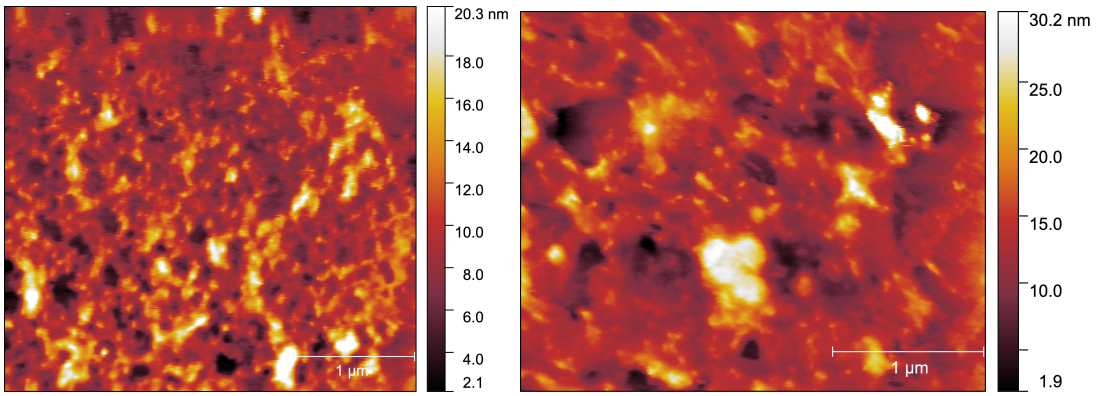


Figure 4.1: AFM topographical images of the sample with 1 day of digestion. Left panel: Dilution 1. Right panel: Dilution 2.

As expected, no CNFs were found, since it was the first day of digestion, but the image blur proved that Zeihr cantilever is not the best choice for this type of samples. Even so, dilution 2 seemed to be somewhat closer to CNFs.

PPP-FMR Cantilever

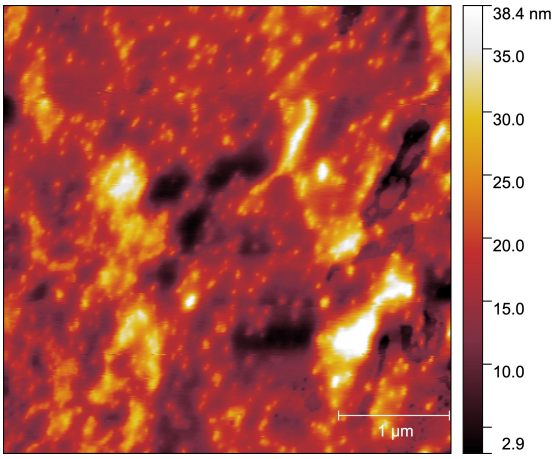


Figure 4.2: AFM topographical image of dilution 2 with 2 days of digestion.

Slight evidence of a CNF was spotted in the top right of 4.2, using PPP-FMR cantilever. Notice that it was the second day of digestion. The resolution of the images obtained with this cantilever was superior than Zeihr's. A cross section cut was taken from the image, in order to study the height of the possible CNF evidence.

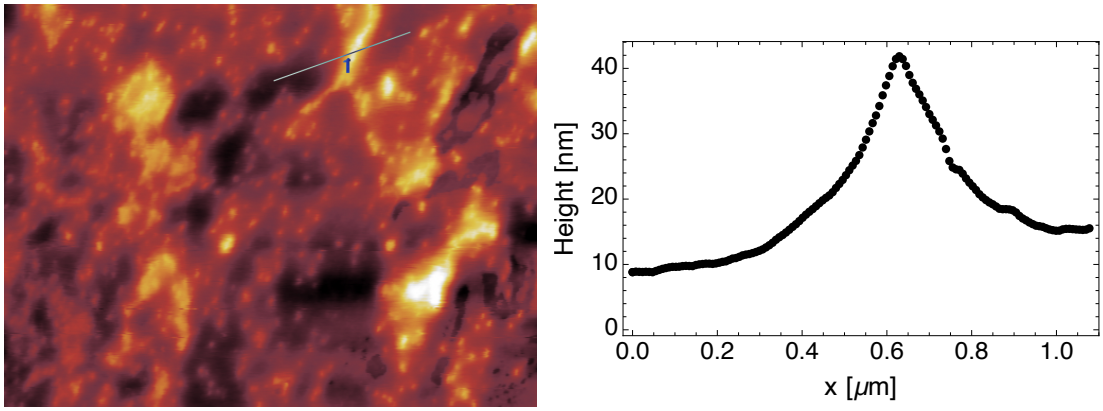


Figure 4.3: Left panel: Cross sectioned image of the zone presented in Fig. 4.2. Right panel: Height distribution of the cross-sectioned zone.

It is directly noticeable from Fig. 4.3 that the background is not flat, instead, the fiber seems to be on a film with roughness on the scale of tens of nanometers. Considering this, we tried creating more diluted samples. Also, the height of the CNF seemed to be of at least 20 [nm] above the film, and considering the results seen in literature, as presented in Ch. 1, this probably corresponds to a fiber cumulus.

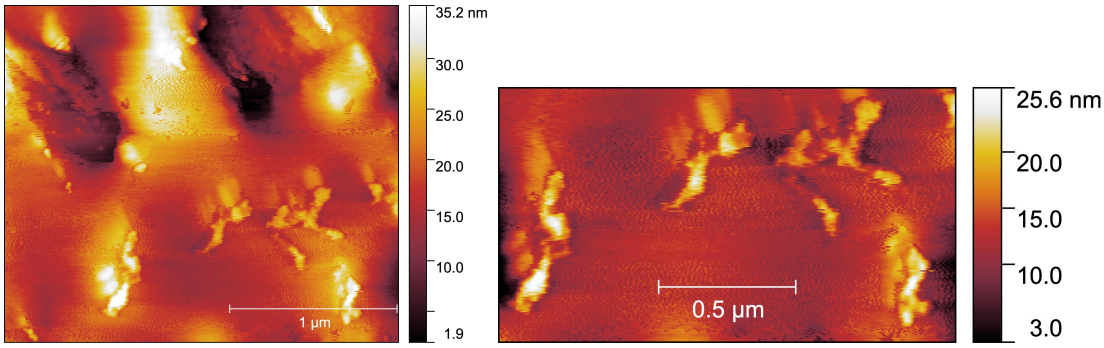


Figure 4.4: AFM topographical images of dilution 2 with 3 days of digestion, done with PPP-FMR cantilever. Right panel is a zoom of left panel image.

In Fig. 4.4, more fiber-like structures were spotted. Again, a film seemed to be behind them. A height distribution was taken from the right panel image, presented in Fig. 4.5.

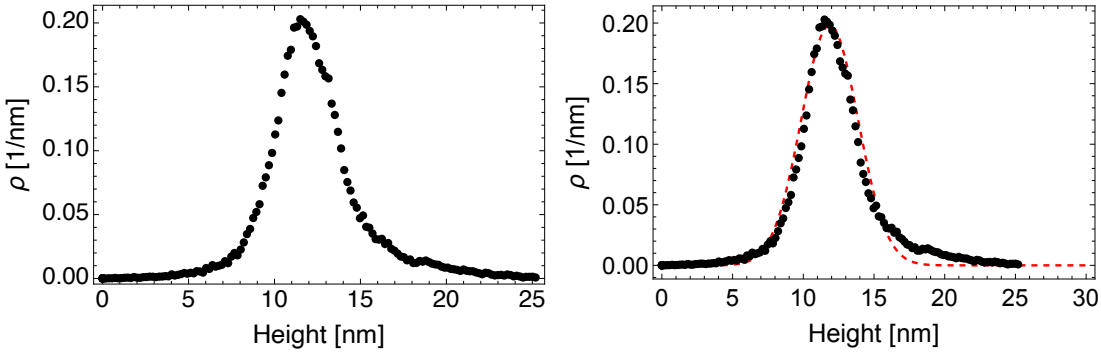


Figure 4.5: Left panel: Height distribution of the right panel image from Fig. 4.4. Right panel: Same as left panel, but with a Gaussian fit in red-dashed lines.

Height distribution shows one clear and big peak, as well as one tiny peak. The distribution center is around 12±2[nm] (following the Gaussian Fit), and should account for the background, while the smaller peak, that is around 181[nm], should correspond to the "CNFs". It is difficult to conclude the fibers' height, since they could be mixed with the background film, above it, or at silicon, with the film just surrounding them.

SSS-FMR Cantilever

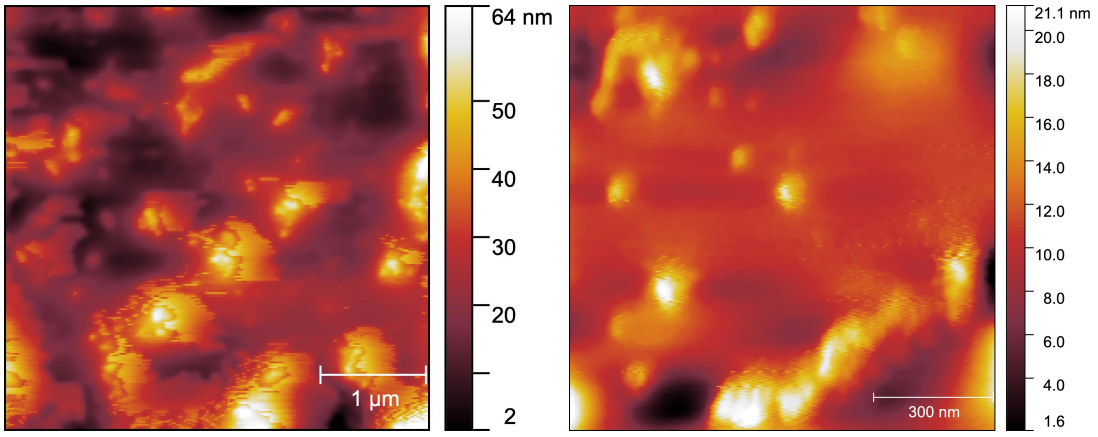


Figure 4.6: Left panel: AFM topographical image of dilution 2 sample with 3 day of digestion. Right panel: Zoom of the left panel's zone.

With the use of SSS-FMR tips, the resolution increased considerably, to the point that individual fibers in a scale of 1x1[μm] could be spotted.

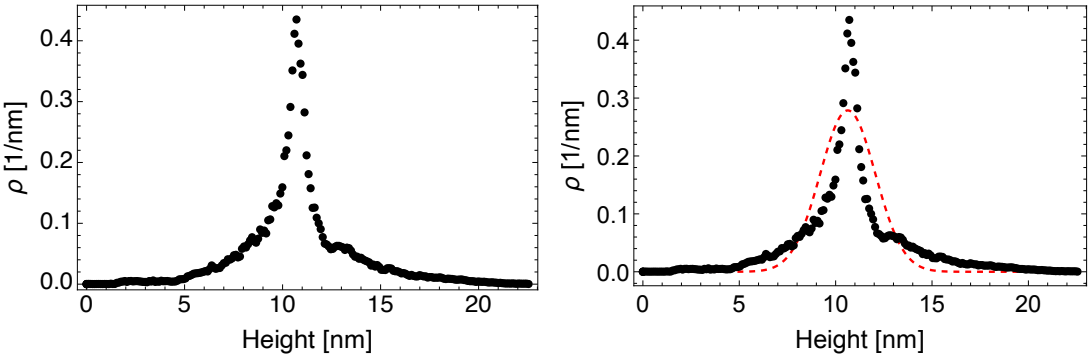


Figure 4.7: Left panel: Height distribution of the right panel image from Fig. 4.6. Right panel: Same as left panel, but with a Gaussian fit in red-dashed lines.

The fit did not overlay perfectly to the original data, but it is useful to identify where the center of the density is located. The center of this distribution of height is around 11±1[nm], which accounts for the background, while the fibers are probably the little peak that is around 13[nm]. Once again, the background film is a problem. Before changing to phase 2, one last region of dilution 2 sample was studied, and force spectroscopy was done on it.

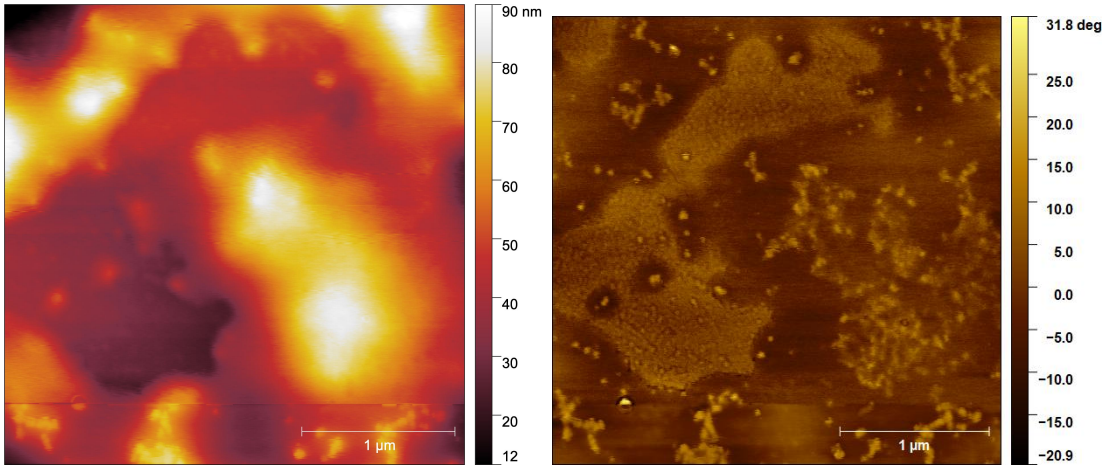


Figure 4.8: Left panel: AFM topographical image of a zone of dilution 2. Right panel: AFM phase contrast image of the same zone as left panel.

In Fig. 4.8 (right panel), a phase contrast image is presented. Phase contrast plots differences of energy dissipation between the points of the map. Many reasons can cause contrast in the phase image, but in this case, it could be due to the stiffness-difference of the surface points. Phase image can be used as a qualitative indicator of the surface's morphology. In fact, in Fig. 4.8, the phase image shows sharper details than the topography one.

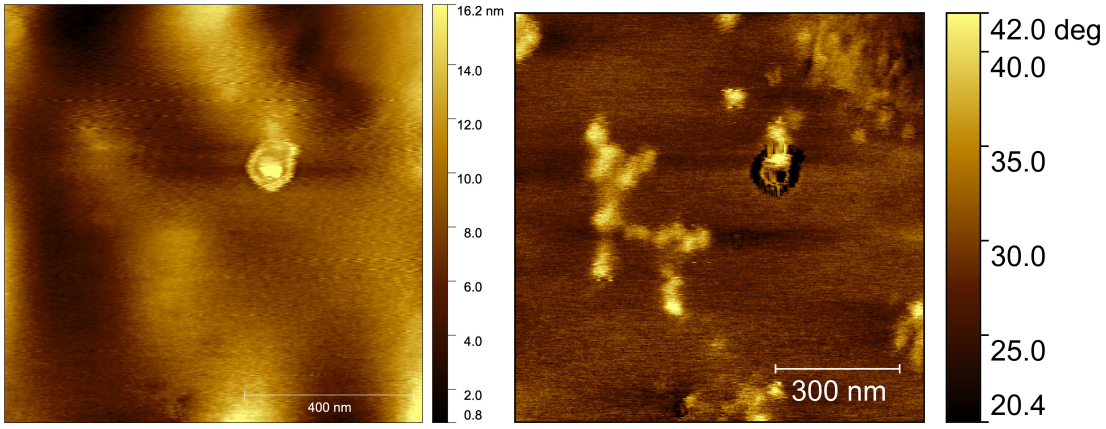


Figure 4.9: Left panel: AFM topographical image zoom of zone presented in Fig. 4.8. Right panel: AFM phase contrast image of the same zone as left panel.

In Fig. 4.9 a big diffence between the image-quality of topography and phase mode is visible. As in phase contrast mode, a fiber-like structure was spotted, force spectroscopy was done in the zone, in order to see if there was any indentation on the force distance curves, and to have an idea of the sample's Young's modulus.

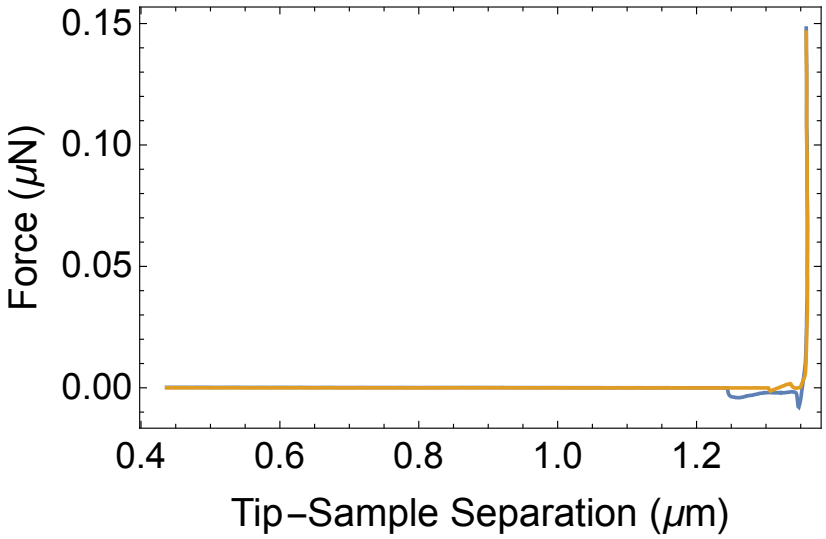


Figure 4.10: Force curve taken from the force spectroscopy of zone presented in Fig. 4.9. Approach in orange, retract in blue. This is an example of force curve on a point of the background.

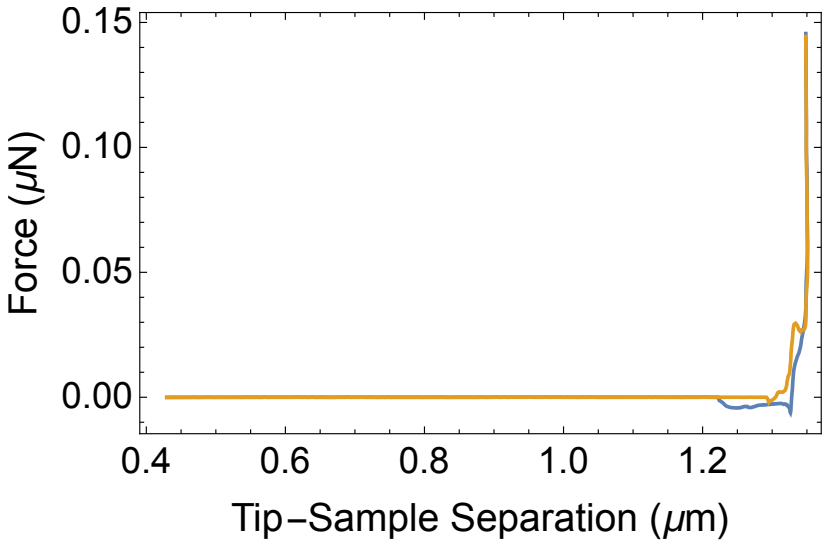


Figure 4.11: Force curve taken from the force spectroscopy of zone presented in Fig. 4.9. Approach in orange, retract in blue. This is an example of force curve on a point of the Fiber-like structure.

Fig. 4.11 does not show any indentation, as it correspond to silicon. Fig. 4.10 present indentation, as it correspond to CNF. Seeing Fig. 4.8, it is not difficult to see that the fibers are on a film, or at least surrounded by them, so, force curves having indentation does not necessarily imply that fibers were deformed. Even considering that, this experiment was very important in the context of the present research, since it was the first time that force spectroscopy was realized on CNF's samples. Also, it opened the door to study the Young's modulus of surfaces with analysis softwares, applying the Hertz Model as explained in Chapter 2. The Young's modulus map of this experiment (Fig. 4.12) did not correlate with the image's topography, so no quality information could be obtained.

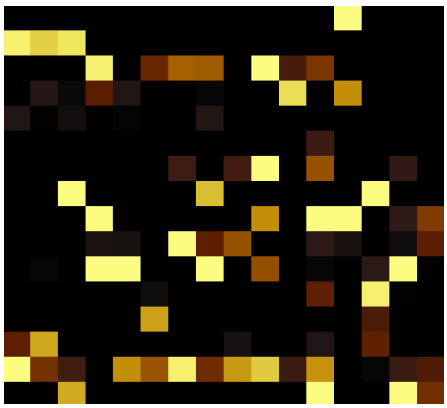


Figure 4.12: Young's modulus' map of the zone presented in Fig. 4.9

4.1.2 Second Phase

This phase is characterized by the use of only SSS-FMR cantilever, with the characteristics described in Sec. 4.1.1. The protocol followed to create the samples was the one presented in Chapter 3, and 3-dfg samples were analyzed as well as the control ones. Variations of relative humidity were also added by this part.

Control Samples Imaging without HC

First, results on control samples **without** controlled humidity are shown below.

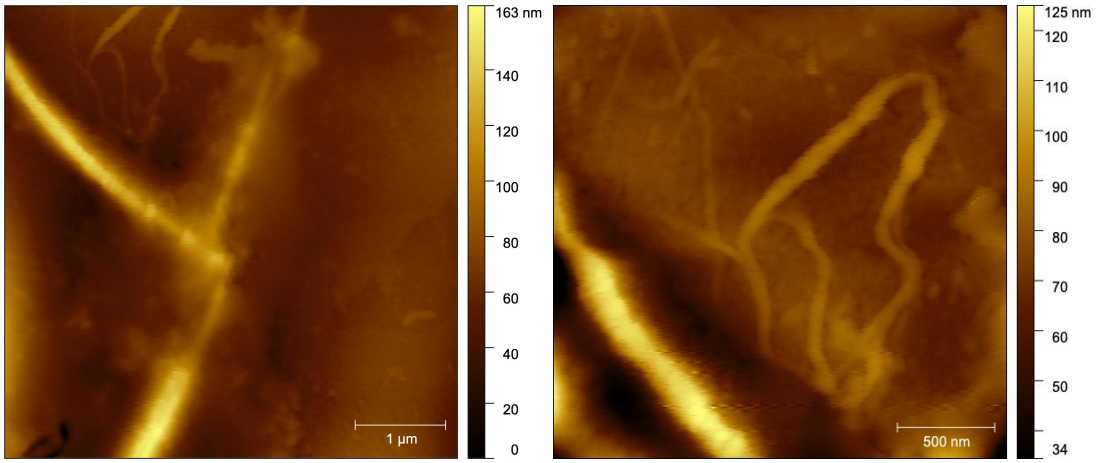


Figure 4.13: AFM topographical images of the sample with 1 day of digestion and 1:500 dissolution. Left panel: 5x5[μm^2] image, right panel: Zoom of the top-left part of the same region.

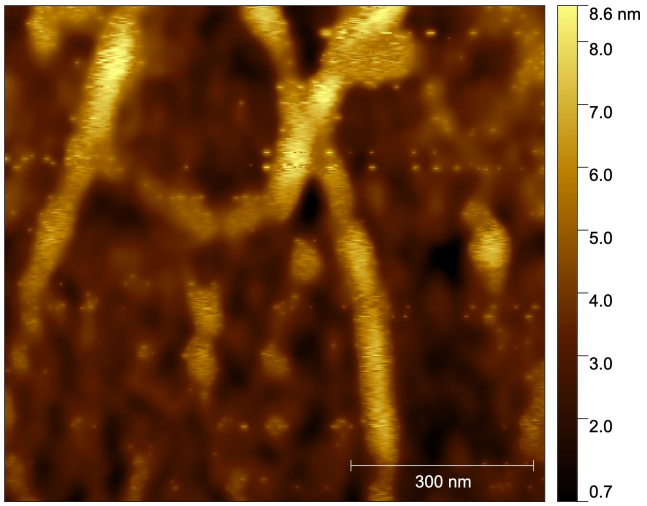


Figure 4.14: AFM topographical image zoom of the zone presented in Fig. 4.1.

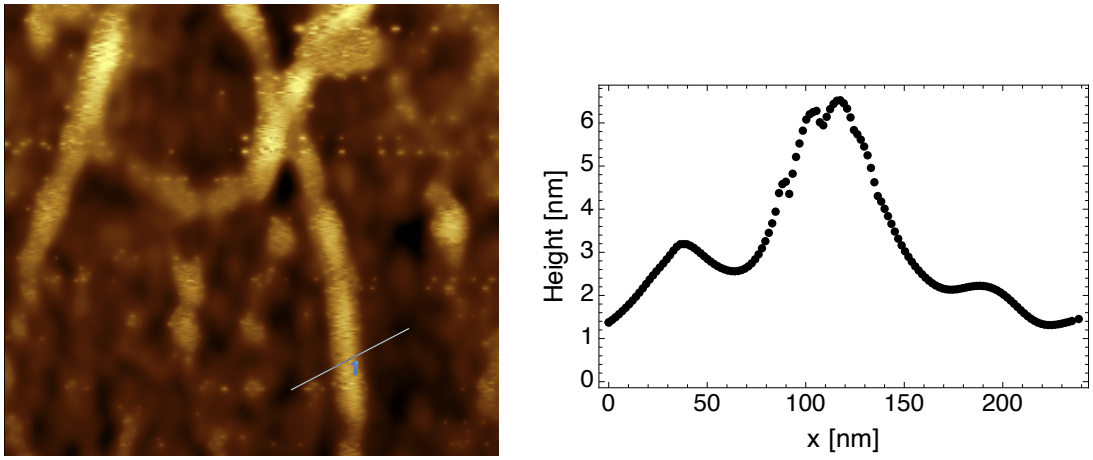


Figure 4.15: Left panel: Cross sectioned image of the zone presented in Fig. 4.14. Right panel: Height distribution of along the cross section.

In Fig. 4.15, by measuring the highest peak along the cross section, a height around 4[nm] for the fiber is shown. The cross section shows two peaks, which suggests some irregularities on the background. Probably the sample was not diluted nor digested enough, since the fiber seemed to be mixed with the background, that does not look like clean silicon.
By day 3 of digestion, finally more individualized fibers were spotted, with a visible rod-like shape and a cleaner silicon background.

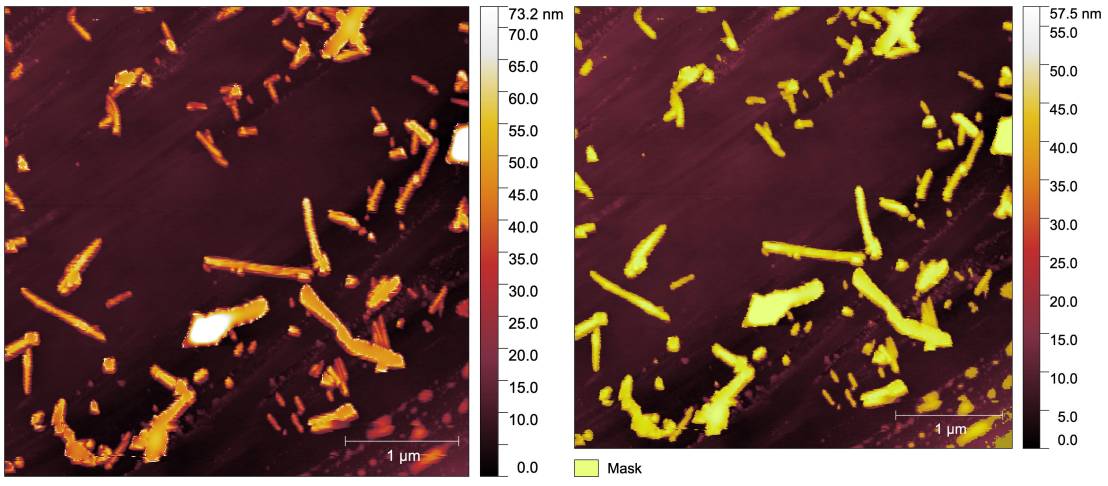


Figure 4.16: Left panel: AFM topographical image of the sample with 3 days of digestion and 1:500 dissolution. Right panel: Same zone of left panel, with a Mask filter on height (most of fibers included).

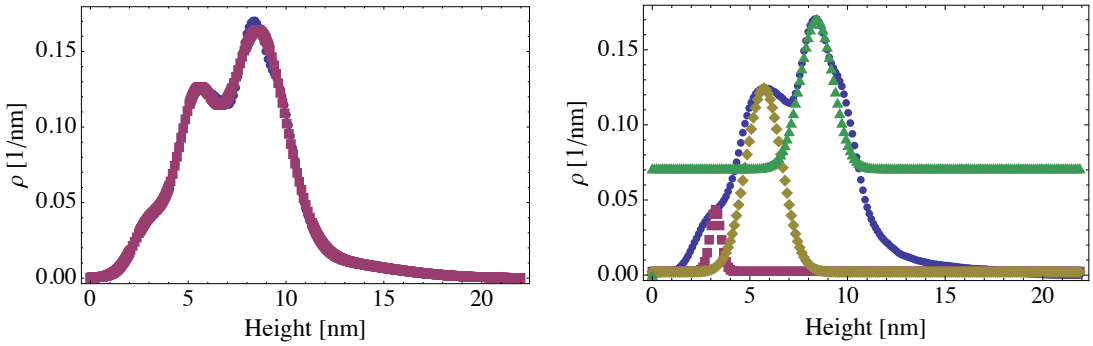


Figure 4.17: Left panel: Height distribution of the masked zone presented in Fig. 4.16, with a fit in cherry color points. The fit is composed by a sum of three Gaussians. Right panel: Decomposition of the fit presented in left panel.

By the fit, 3 different heights for fibers were found, with peaks around 3,5, and 8±3[nm]. The standard deviation, even though is big compared to the height, is reasonable, since we could see that the final fit could be divided in three gaussians (Fig. 4.17). This can be interpreted by the pressence of fibers that are more digested than others, or that some are completely isolated, while others could be a kind of cumulus. Also, there still is a film on the background, affecting the measurements. Another zone of the same sample was studied, which is presented in Fig. 4.18.

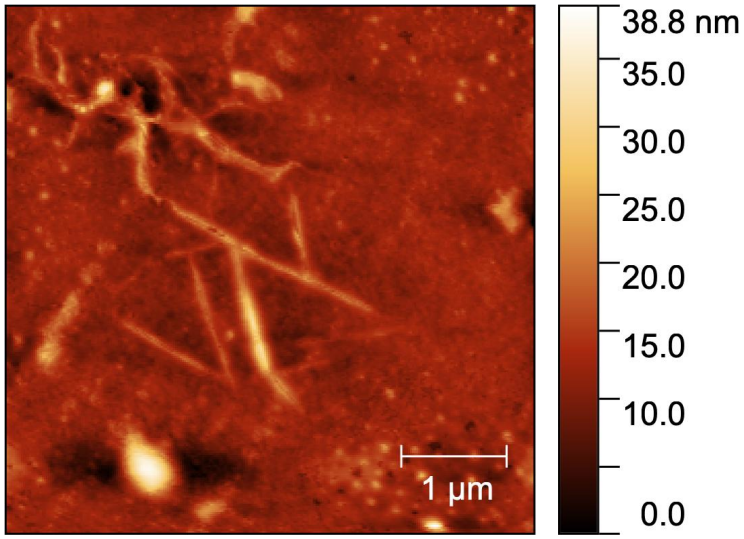


Figure 4.18: AFM topographical image of the sample with 3 days of digestion and 1:500 dissolution.

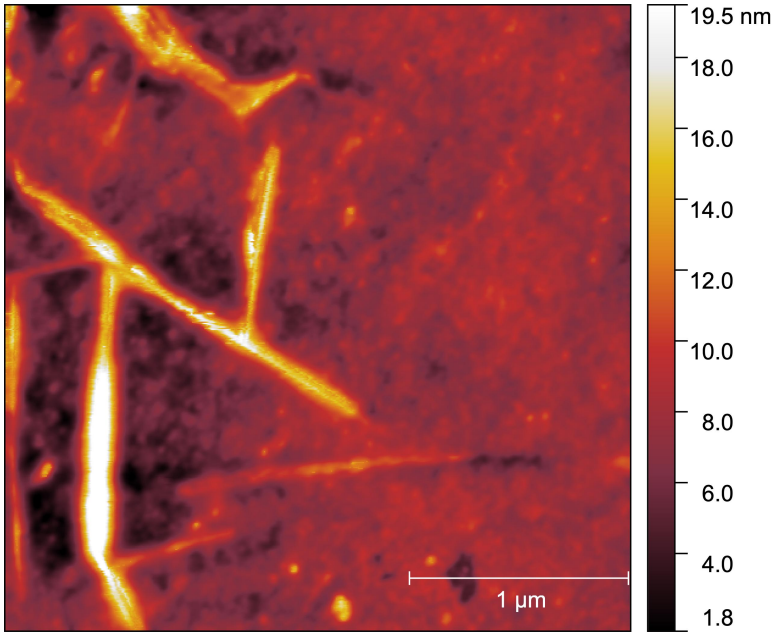


Figure 4.19: AFM topographical image zoom of the zone presented in Fig. 4.18.

As in Fig. 4.19 the background seemed cleaner, a height distribution of the entire zone was taken, which is presented on Fig. 4.20. Fitting the distribution to a Gaussian, a medium height of 8.23[nm]±1.46[nm] is obtained for the entire image.

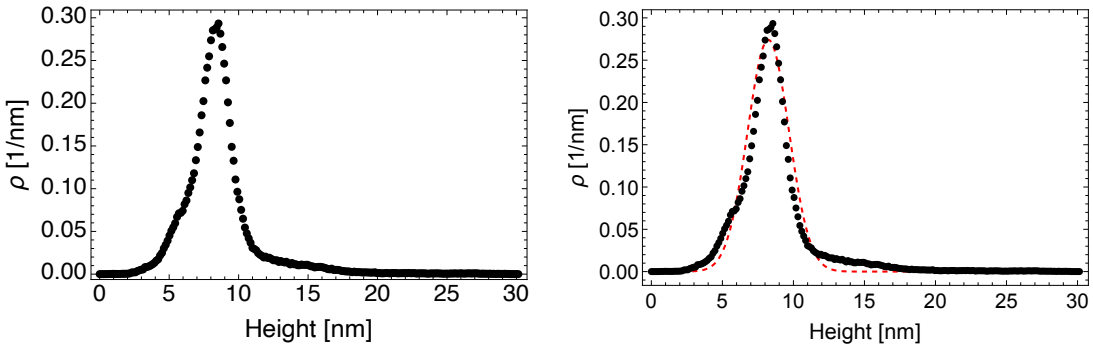


Figure 4.20: Left panel: Left panel: Height distribution of Fig 4.19 zone. Right panel: In dashed-red lines, the Gaussian fit of the height distribution presented in left panel.

This distribution center does not seem to account for the fibers. The same is observed in Fig. 4.5, but in this case, there are three different peaks. The peak that the gaussian fits seems to be thanks to the background. In fact, if we put a height mask over the region with fibers and see the height distribution without it, the results show some equivalence (Fig. 4.21).

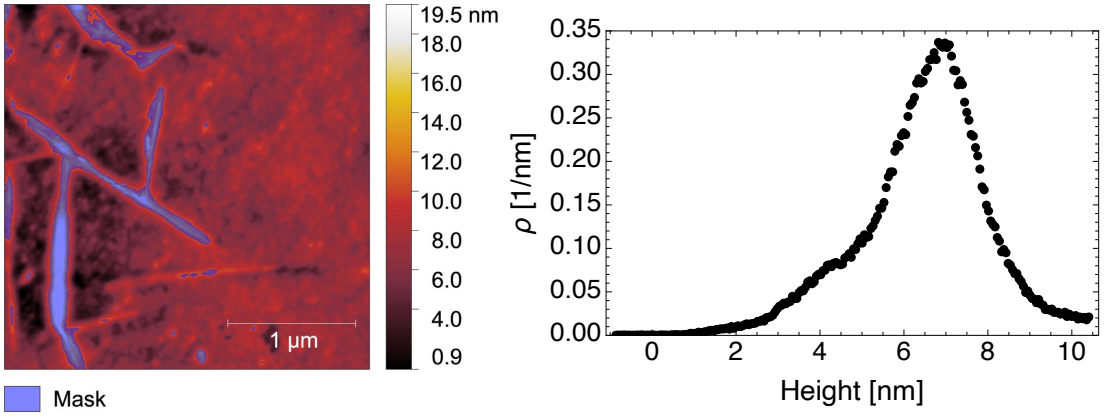


Figure 4.21: Left panel: Same image as Fig. 4.19, but with a mask filter (purple). Right panel: Height distribution of the zone without mask on the left panel.

Individual fibers were spotted, which is the first important goal of this work. The next step was to apply force spectroscopy to those fibers and then add the humidity chamber. Another zone with fibers was spotted and force spectroscopy was done on it, applying 130[nN] of maximum force.

Control Samples Force Spectroscopy without HC

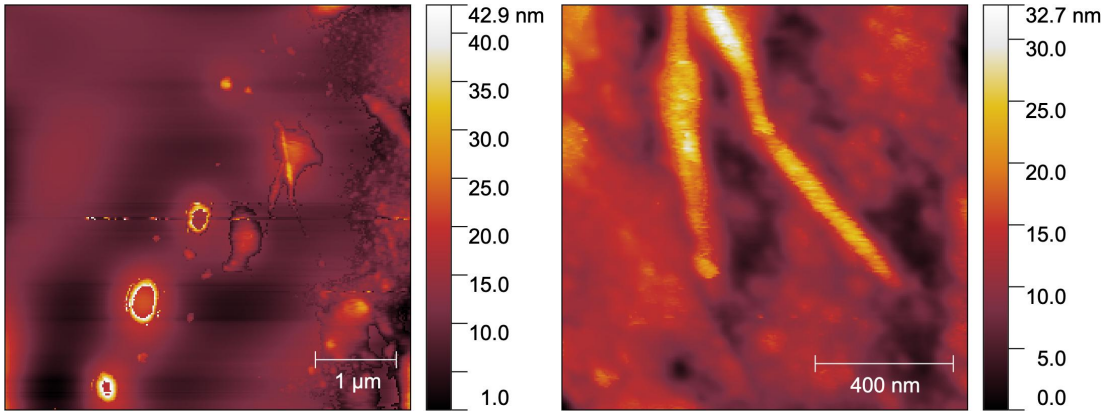


Figure 4.22: Left panel: AFM topographical image of the sample with 3 days of digestion and 1:500 dissolution. Right panel: Zoom on left panel zone.

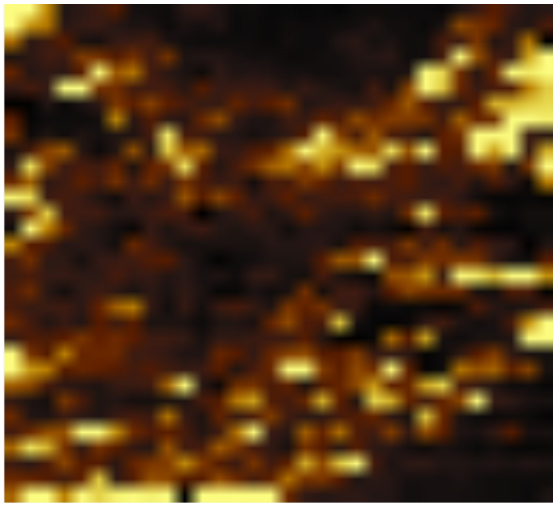


Figure 4.23: Young's Modulus' map of the force spectroscopy experiment, presented in Fig. 4.24.

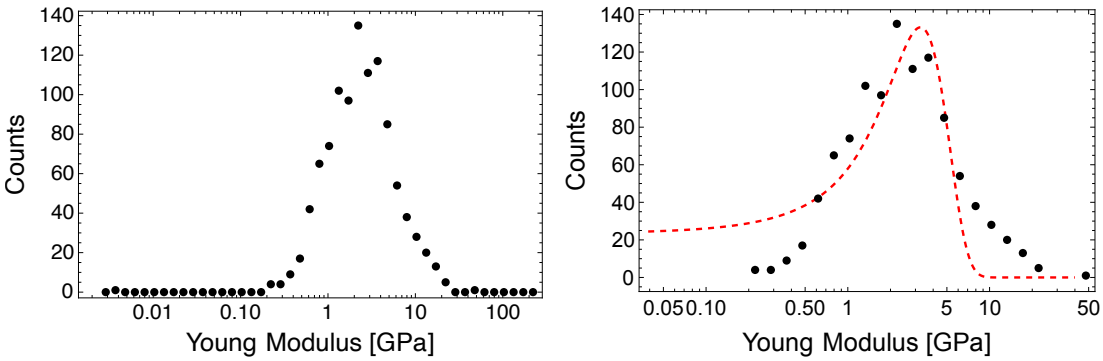


Figure 4.24: Left panel: Young Modulus' Histogram of the force spectroscopy on the zone presented in Fig. 4.22. In dashed-red lines, Gaussian fit of left image graphic, where points with value 0 in counts axis have been ignored.

The distribution center shows a Young's modulus of around 3±2[GPa]. The high standard deviation is not a surprise, since the map of Young modulus generated with the force spectroscopy, did not well represented the fibers that were expected to be spotted (Fig. 4.24). This could be caused by the time taken between the topographical image and the force spectroscopy. The sample region is small, and the AFM is not fully isolated from the environment, so any external perturbation can produce thermal drift, which changes the position of the sample.

Even though the force spectroscopy experiment did not show conclusive results, a difference in the force curves of silicon and celullose was noticeable, as shown in Fig. 4.25.

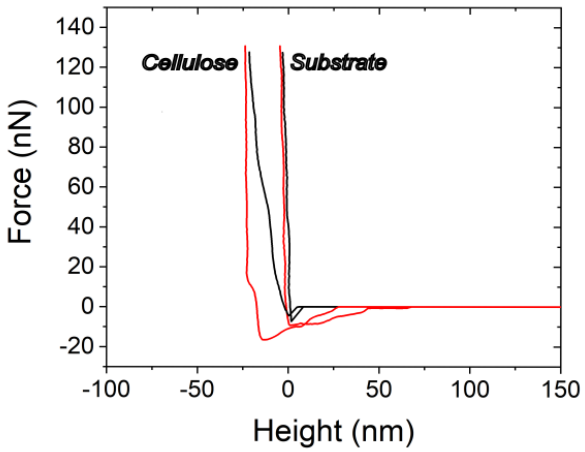


Figure 4.25: Two force curves taken from the experiment on the zone presented in Fig. 4.22. In black the approach, and in red the retract.

Control Samples Imaging and Force Spectroscopy with HC

The last two experiments performed on control samples centered on measuring to stiffness and swelling of the nanofibers, under variable relative humidity.

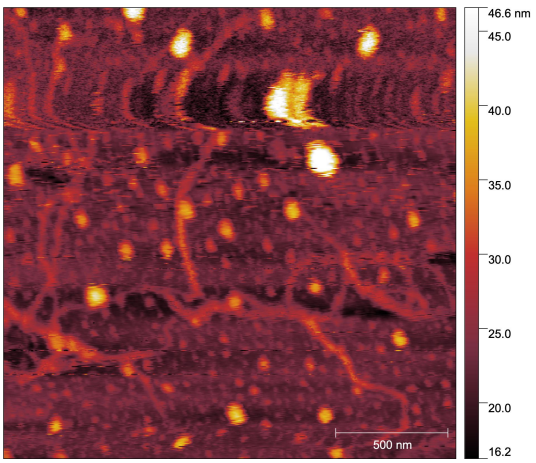


Figure 4.26: AFM topographical image of the sample with 3 days of digestion and 1:500 dissolution, and between 54±4% RH. The image evidences a drift due to change in pressure inside the hc.

While the image presented in Fig. 4.26 was being taken, the flow of gas within the humidity chamber was varying, in order to see if it was possible to maintain a spot while modifying it. A drift was evidenced towards the top of the image, but the zone was not lost. Force spectroscopy map was taken on the zone, pressing with a maximum force of 250[nN], getting a Young Modulus' map that evidenced the difference between fibers and the background.

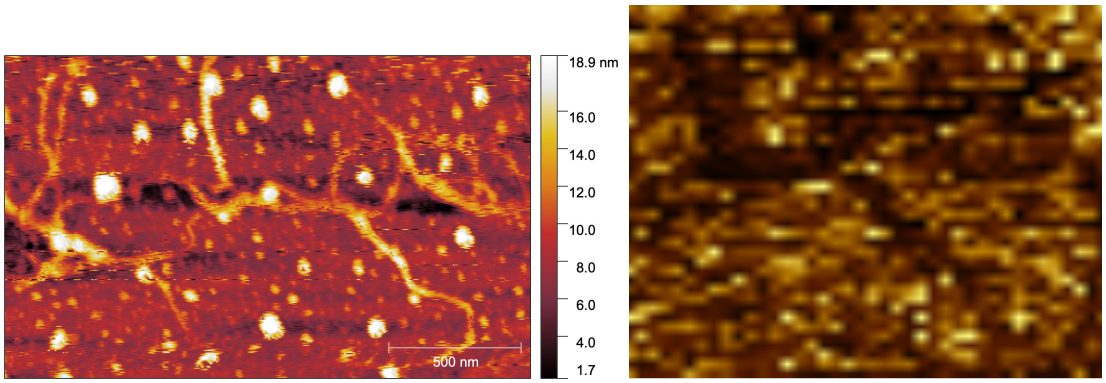


Figure 4.27: Left panel: AFM Topographical image of the zone where force spectroscopy was applied, at 54±4%RH. Right Panel: Young modulus' map of the zone in the left panel. The zone studied was the middle-right part of left panel.

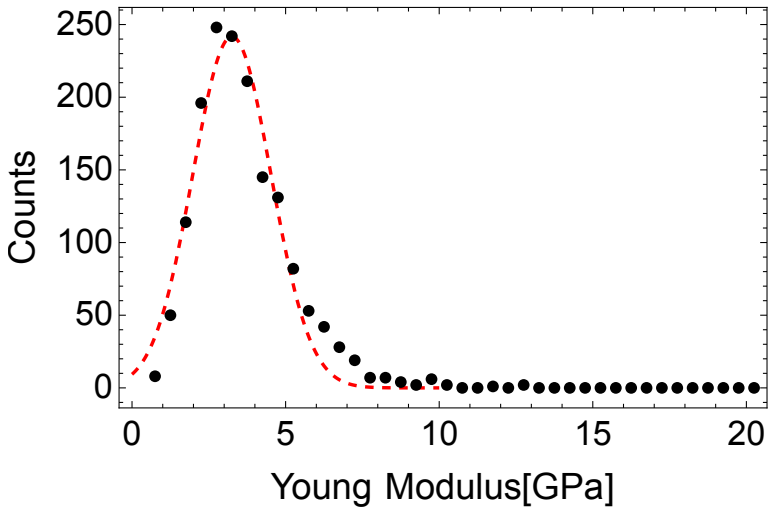


Figure 4.28: Young Modulus' Histogram of the force spectroscopy of entire map the zone presented in Fig. 4.27, with 54±4% RH. In dashed-red lines, a gaussian fit.

From the fit of Fig. 4.28, a Young Modulus median of 3.251[GPa] can be extracted.

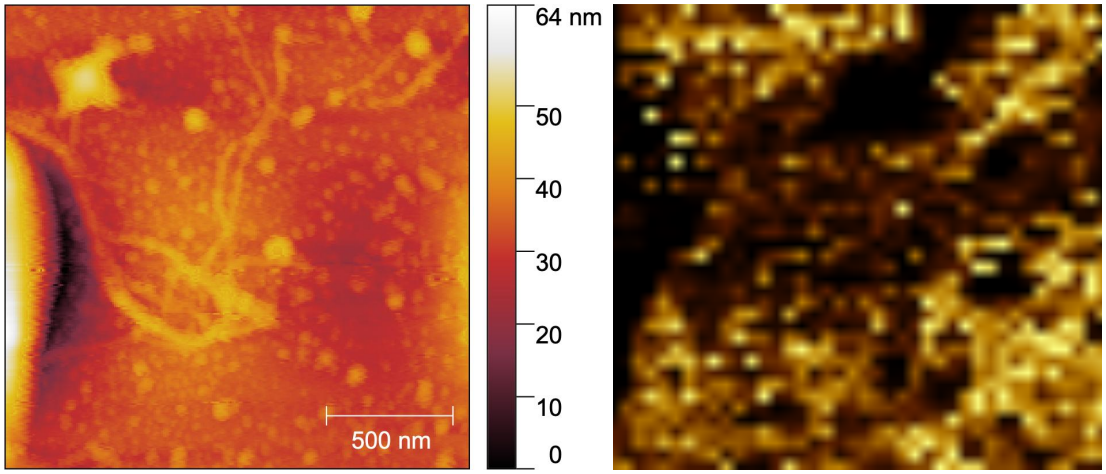


Figure 4.29: Left panel: AFM Topographical image of the zone where force spectroscopy was applied, at 4±1%RH. Right Panel: Young modulus' map of the entire zone in the left panel.

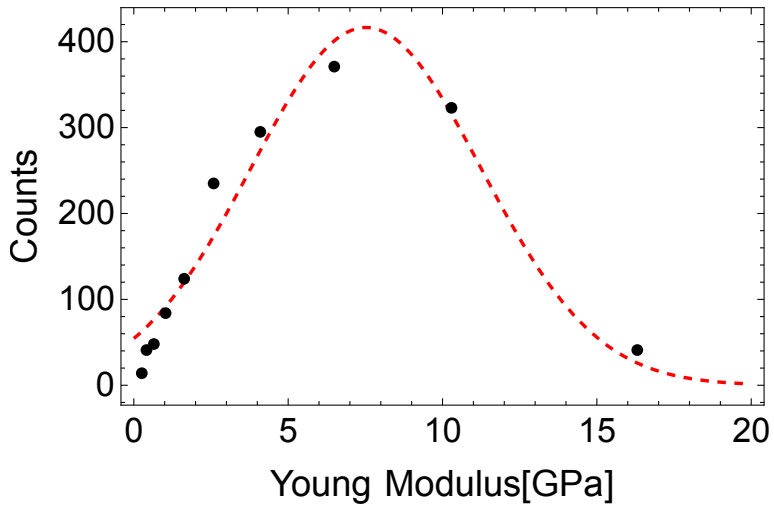


Figure 4.30: Young Modulus' Histogram of the force spectroscopy on the zone presented in Fig. 4.29, with 4±1% RH. In dashed-red lines, a gaussian fit.

The interesting part of this is that although the fibers seem different, the zone should be the same. Doing experiments, it was not difficult to note that the fibers were affected with every force spectroscopy that was applied. When the tip pushes the sample, the sample is displaced. That could be the reason of this new array, and is also the reason why another experiment was needed to study the swelling of the fibers, using only imaging.

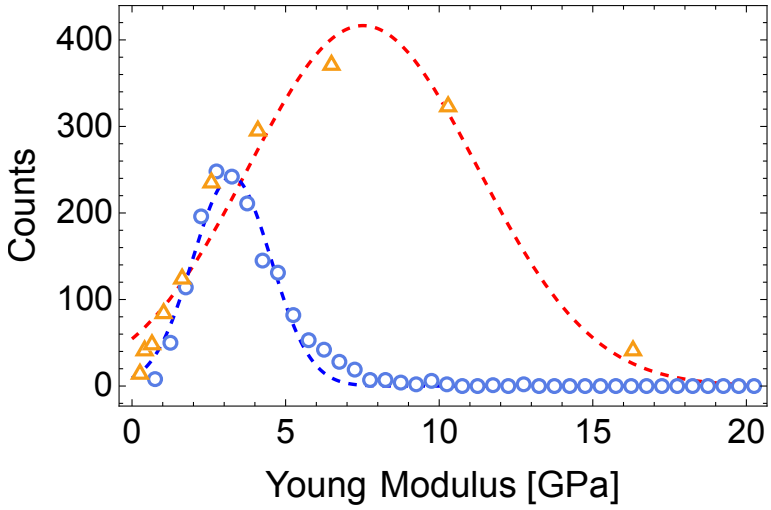


Figure 4.31: Young Modulus' Histogram of force spectroscopy experiments done in the same zone, with 4±1% and 54±4% RH on the control sample. In orange/red is the data and gaussian fit of the experiment with 54%RH, while 4% RH is in blue.

Fig. 4.31 shows a tendency for the Young's modulus to increase with the decrease of the relative humidity. Although, the standard deviation of both fits is considerable. For this reason, the greater gaussian covers all the region where the tinier lives, not allowing to obtain concrete conclusions. A reason that can cause this is that the Young's modulus that were plotted made account of the full images shown in Figs. 4.27 and 4.29.
In order to reduce the high deviation of the mechanical maps, masks were generated on them on them, aiming to take into account only the fibers of the region of interest. Results of this process are shown in Figs. 4.32 and 4.33.

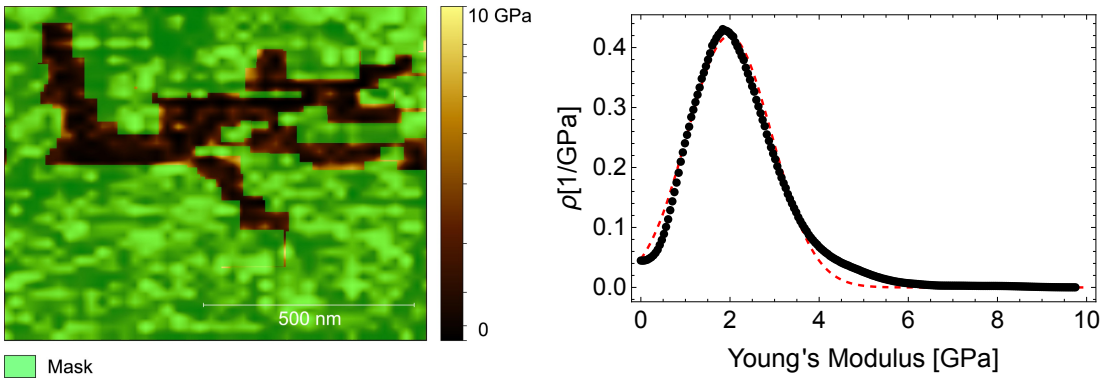


Figure 4.32: Left panel: Mask (green) applied to the Young's modulus' map presented in Fig. 4.27, corresponding to 54% RH. Right panel: Young's modulus distribution of the non-masked region of left panel.

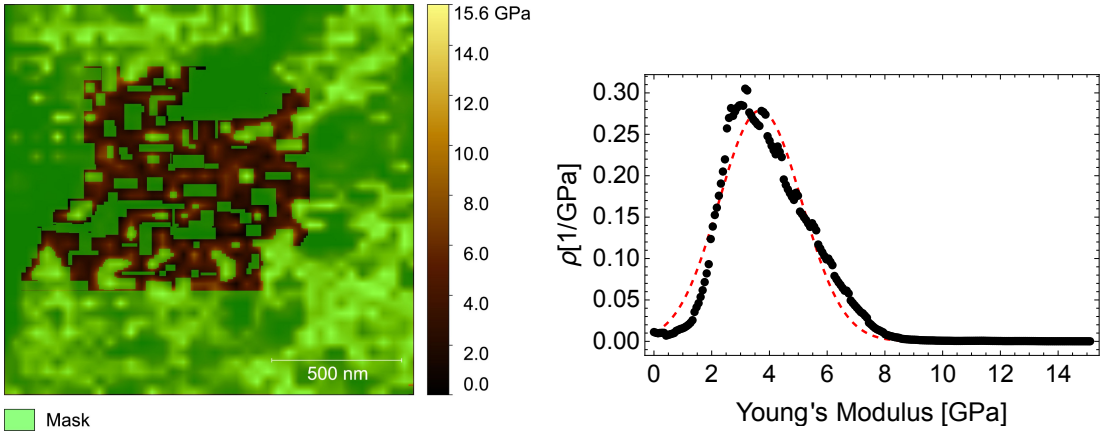


Figure 4.33: Left panel: Mask (green) applied to the Young's modulus' map presented in Fig. 4.29, corresponding to 4% RH. Right panel: Young's modulus distribution of the non-masked region of left panel.

The mask allows to study only the regions of interest that an image has. The regions of interest were unmasked. The new plot of both distributions, as in Fig. 4.31, is shown in Fig. 4.34.

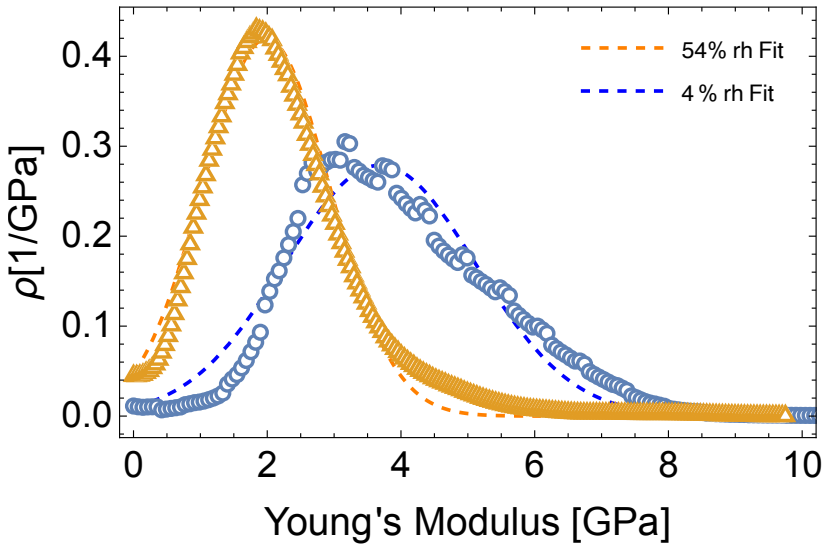


Figure 4.34: Young's Modulus' distribution of the non-masked regions presented in Figs. 4.33 and 4.32. In orange is the data and gaussian fit of the experiment with 54±4%RH, while 4±1% RH is in blue.

Fig. 4.34 shows in a better way that, in fact, the Young's modulus of control nanofibers seems to increase with the decrease of relative humidity. Gaussian fits for 4% and 54% RH yield a Young's Modulus of 3.7±1.4[GPa] and 2.0±1.0[GPa], respectively.

As the fibers seemed to change its form once force spectroscopy was made, the changes on morphology could not be appreciated. For this reason, experiments with variable relative humidity but only on imaging mode were applied. Topographical images of a control sample with 3 days of digestion and a dilution of 1:500 were taken, as presented in Fig. 4.35.

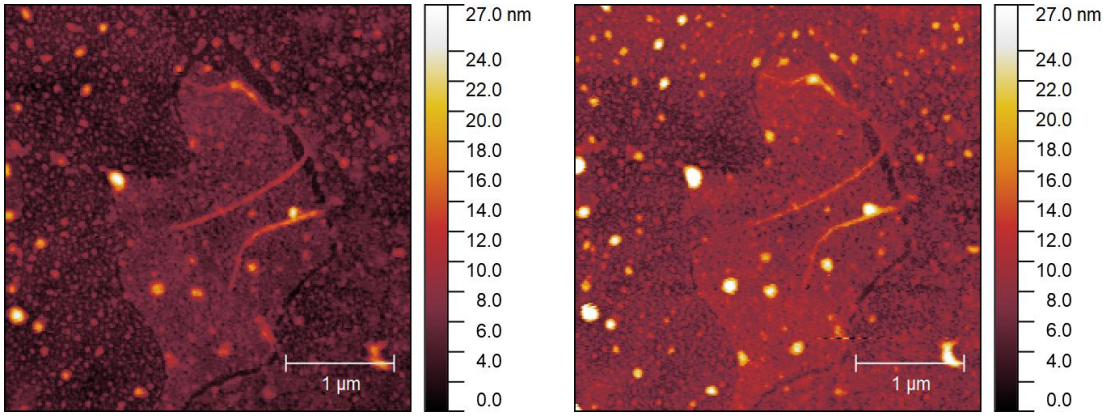


Figure 4.35: Region of the control sample analyzed. Left panel: The sample had been 20 minutes at 6% RH. Right panel: panel: The sample had been 30 minutes at 55% RH.

To analyze the change on morphology of a single fiber, masks were put on a fiber selected (Figs. 4.36 and 4.37).

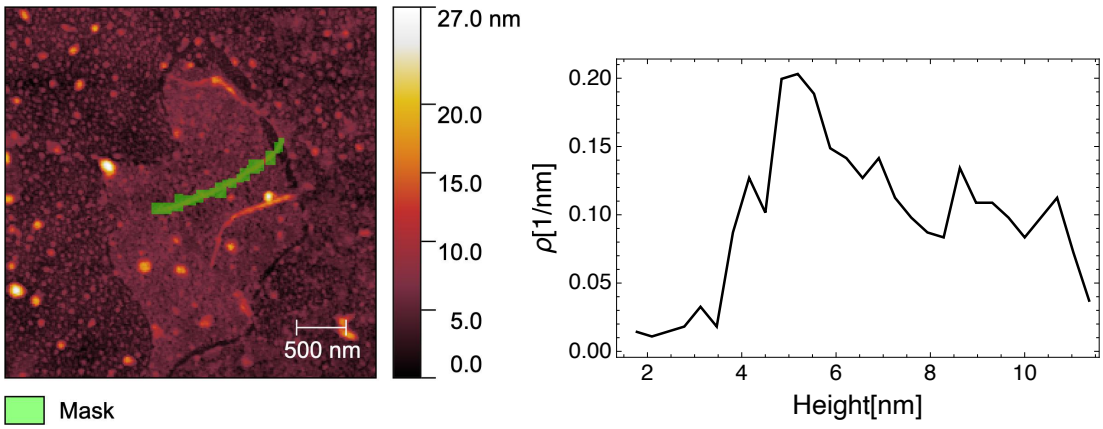


Figure 4.36: Left panel: Region of the control sample analyzed. The sample had been 20 minutes at 6% RH. A mask (green) is put on a single fiber observed. Right panel: Height distribution of the masked region.

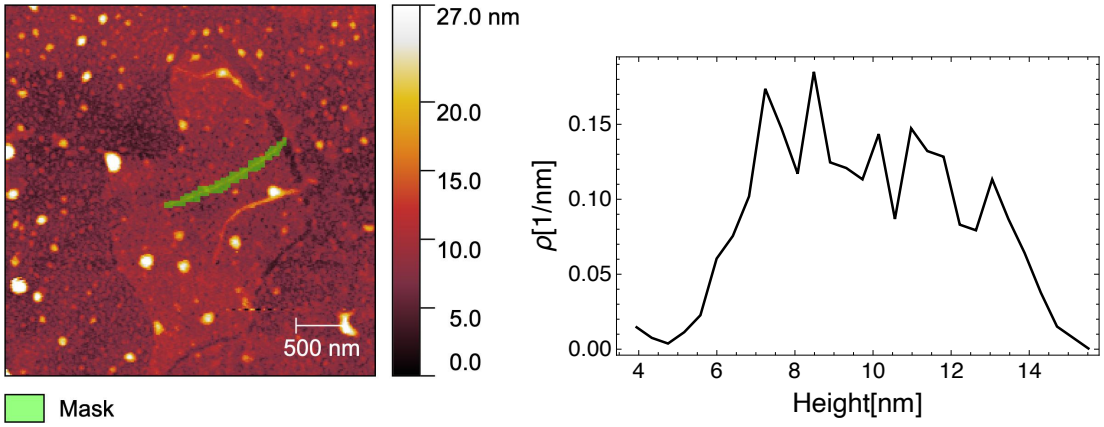


Figure 4.37: Left panel: Region of the control sample analyzed. The sample had been 30 minutes at 55% RH. A mask (green) is put on a single fiber observed. Right panel: Height distribution of the masked region.

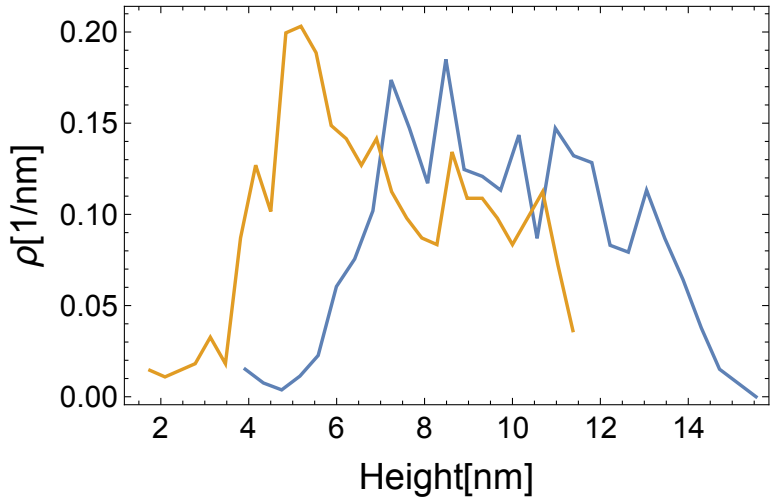


Figure 4.38: Height distribution of the masked fiber presented above. In orange, 6% RH. In blue, 55% RH.

From Fig. 4.38, we can conclude that the control fibers seems to change their morphology with the change of relative humidity. They may swell as exposure to water increases. With this result, control fibers were shown to absorb water by two different analysis: morphological and mechanical (Fig. 4.34). Nevertheless, the effect that is shown in Fig. 4.38 could be due to a general swell of the sample, which would include the film where the fibers is placed on. If that were the case, Fig. 4.38 would not be an absolute prove of the CNF's swelling. This possibility increases as we can see in Fig. 4.35 that the images are on the same scale, but in the case with more humidity, the entire region seems to be at higher height.

3dfg Samples

The samples that were modified with 3dfg molecules were analyzed with AFM, and interesting results were obtained, compared to the control sample.

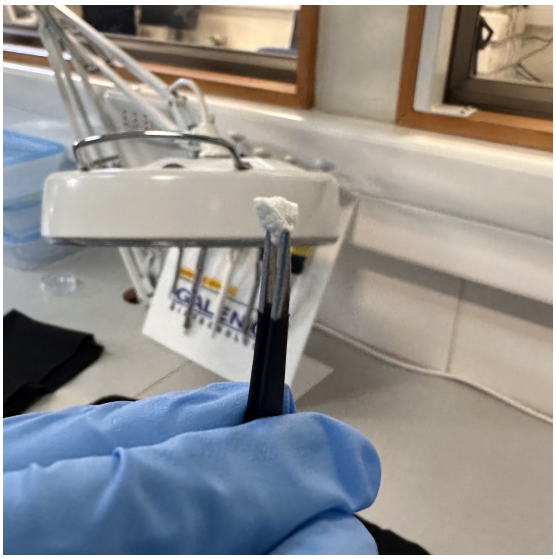


Figure 4.39: Photography of the 3dfg sample studied, before the digestion process.

The fist interesting thing to note in Fig. 4.39 is that 3dfg sample was similar to a cotton, but hardly compressible by tweezers. It felt mechanically harder than control sample.



Figure 4.40: Comparison of control (left) and 3dfg (right) samples with one day of enzymatic digestion.

In Fig. 4.40, it is visible that both samples behave differently inside the same dilution. The control sample **dilutes**, while 3dfg seems to **absorb** the solvent. To begin the AFM analysis, we took a sample with two days of digestion, generated using the same protocol as in control samples (Chapter. 2), i.e. a drop of solution was dried above silicon.

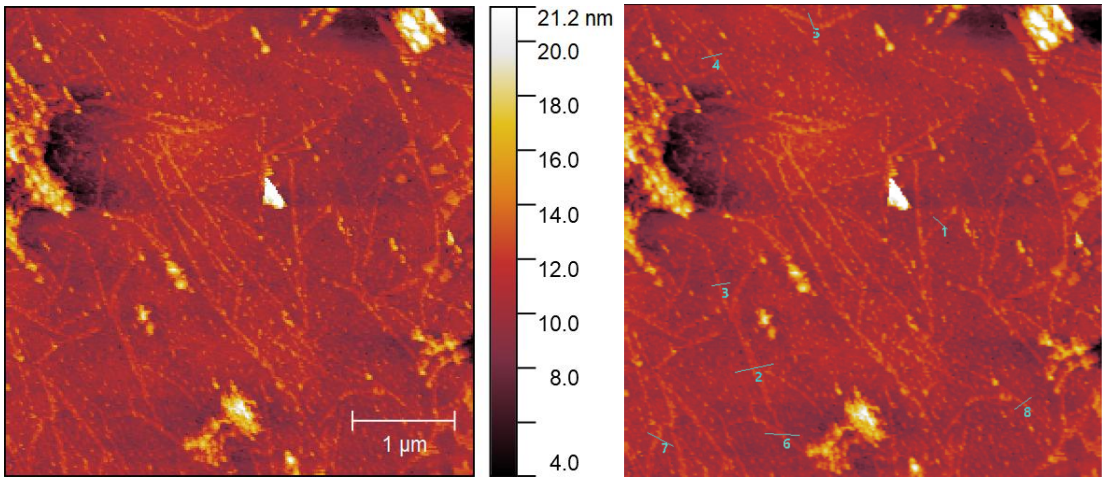


Figure 4.41: Left panel: Topographical image of 3dfg sample with 2 days of digestion and 1:1000 dilution. Right panel: Same image as Left panel, but with 8 cross sectional cuts taken.

Once digested, the AFM analysis started, finding that samples with two days of digestion and 1:1000 water-diluted had visible nanofibers (Fig. 4.41). It is not hard to see that 3dfg fibers seemed smaller than control ones, which can be seen taking several cross sectional cuts. Two representative graphics of these measurements are presented in Fig. 4.42.

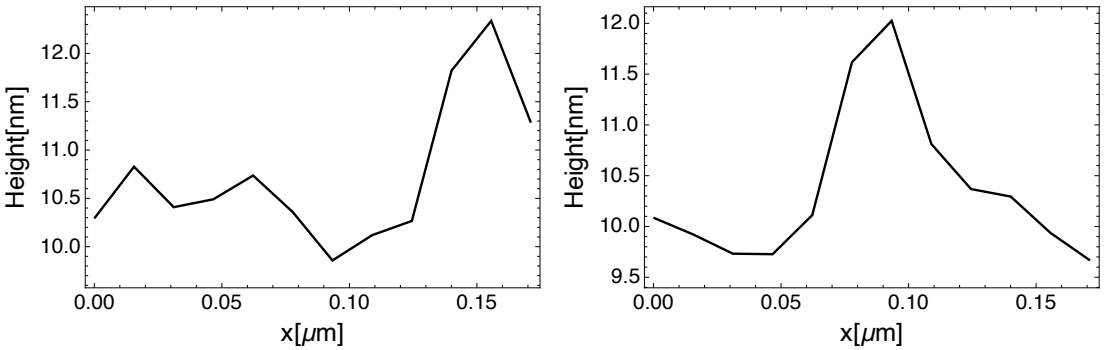


Figure 4.42: Two height measurements taken from the cross sectional cuts of Fig. 4.41. Left: Cross section 2. Right: Cross section 8.

Taking the height shown for every fiber in every cross section graphic, a median height of 2.4±0.6[nm] was found.

4.1.3 Final Discussions

Considering that 3dfg samples should be a mix between control and treated fibers, one hypothesis on these results could be proposed: During the digestion, untreated CNFs that compose the 3dfg sample are making pressure against treated CNFs, and that yields them to be smaller.

In Fig. 4.40, we saw that 3dfg sample absorbed water, but in theory, we were expecting that the Fluorine atom of 3dfg samples yield them to be hydrophobic (not water-absorbent). If the sample is a mix of untreated CNFs that absorbed water (we saw in Fig. 4.38 that they seem to swell with the exposure to water) and treated CNFs (which should not absorb water), the ones that absorbed water and swelled could be creating a pressure on the 3dfg, causing their compression. i.e., as untreated fibers increase their size, 3dfg get pressed against. A little sustain for this theory can be extracted from Fig. 4.41, since only the smaller structures were spotted, but no CNFs with heights comparable to the control ones that were presented before. That could mean that those control CNFs that composed the 3dfg sample may have swollen and became bigger structures. By now, no experiments nor evidence to confirm this has been made/found.

On the other hand, considering the results obtained within this research, a factor that affected all measurements was the a considerable noise and thermal drift. Nevertheless, various representative Young's modulus were obtained and fitted by gaussian distributions, as well as height profiles of CNFs. The results presented are preliminary results of an ongoing investigation, and give us more than a qualitative impression of the materials studied.

In order to get more assertive results, some upgrade on the equipment should be done. As described in chapter 3, our e-AFM does not count with isolation from the environment, such as an acoustic chamber, nor an anti-vibrating table. The addition of such components should improve the quality of measurements, as well as improving the workflow of the experiments themselves.

Experiments on mechanical properties of 3dfg samples were difficult and are not shown, because their dimensions are so small and comparable to the tip radius.

Chapter 5

Conclusions and Outlook

This work explored the synthesis and mechanical analysis of cotton based nanocellulose, using techniques as enzymatical digestion and Atomic Force Microscopy's imaging and force spectroscopy. Additionally, implementation and usage of humidity chamber was made, in order to control the relative humidity of the samples analyzed.

Two different types of cotton based cellulose were studied: Control ones and treated with 3-deoxy-3-fluoro-D-glucopyranose (3dfg) ones. For control cellulose nanofibers, Young's modulus of 3.7±1.4[GPa] and 2.0±1.0[GPa] were found at dry (4±1% relative humidity) and humid (54±4% relative humidity) conditions, respectively. Additionally, experiments suggest that they swell with the increase of relative humidity. A mean height of around 8±3[nm] was also found. Treated 3dfg nanofibers were shown to be smaller than control ones, evidencing a mean height of around 2.4±0.6[nm], which is comparable to the tip radius, a makes the measurements of their mechanical properties more complicated. Macroscopically, treated fibers felt harder than control ones.

Future experiments will focus on the hygromechanical analysis of treated cellulose nanofibers, and their comparison to control cellulose nanofibers.

Bibliography

[1] Steven H Simon. *The Oxford solid state basics*. Oxford Univ. Press, Oxford, UK, 2013.

[2] S. Park, J.O. Baker, and M.E. et al. Himmel. Cellulose crystallinity index: measurement techniques and their impact on interpreting cellulase performance. *Biotechnol Biofuels*, 3(10):0–10, May 2010. ISSN 2731-3654.

[3] Filipe Natalio, Regina Fuchs, Sidney R. Cohen, Gregory Leitus, Gerhard Fritz-Popovski, Oskar Paris, Michael Kappl, and Hans-Juergen Butt. Biological fabrication of cellulose fibers with tailored properties. *Science*, 357 (6356):1118–1122, September 2017. ISSN 0036-8075.

[4] Ishita Chakraborty, Sintu Rongpipi, Indira Govindaraju, Sib Sankar Mal, Esther W Gomez, Enrique D Gomez, Ranjan Dutta Kalita, Yuthika Nath, and Nirmal Mazumder. An insight into microscopy and analytical techniques for morphological, structural, chemical, and thermal characterization of cellulose. *Microscopy Research and Technique*, 2022.

[5] Farah Fahma, Shinichiro Iwamoto, Naruhito Hori, Tadahisa Iwata, and Akio Takemura. Isolation, preparation, and characterization of nanofibers from oil palm empty-fruit-bunch (opefb). *Cellulose*, 2010.

[6] Ming Li, Beihai He, Yiyi Chen, and Lihong Zhao. Physicochemical properties of nanocellulose isolated from cotton stalk waste. *ACS Omega*, 6(39):25162–25169, 2021.

[7] Vegar Ottesen and Kristin Syverud. Swelling of individual cellulose nanofibrils in water, role of crystallinity: an afm study. *Cellulose*, 2021.

[8] Rebecca R. Ruckdashel, Dhanya Venkataraman, and Jay Hoon Park. Smart textiles: A toolkit to fashion the future. *Journal of Applied Physics*, 129 (13):130903, 2021. doi: 10.1063/5.0024006.

[9] Gert R Strobl. *The physics of polymers*, volume 2. Springer, 1997.

[10] Béla Török and Timothy Dransfield, editors. *Green Chemistry*. Elsevier, 2017. ISBN 978-0-12-809270-5.

[11] Langming Bai, Nathan Bossa, Fangshu Qu, Judy Winglee, Guibai Li, Kai Sun, Heng Liang, and Mark R. Wiesner. Comparison of hydrophilicity and mechanical properties of nanocomposite membranes with cellulose nanocrystals and carbon nanotubes. *Environmental Science & Technology*, 51(1): 253–262, 2017. PMID: 27958716.

[12] Jude Okolie, Sonil Nanda, Ajay Dalai, and Janusz Kozinski. Chemistry and specialty industrial applications of lignocellulosic biomass. *Waste and Biomass Valorization*, 12, 05 2021.

[13] `https://pubchem.ncbi.nlm.nih.gov/compound/3-Fluoro-3-deoxy-D-glucopyranose`. Accessed: 2023-2-28.

[14] Chi Zhang, Mingyang Chen, Benoit Coasne, Sinan Keten, Dominique Derome, and Jan Carmeliet. Hygromechanics of softwood cellulosic nanocomposite with intermolecular interactions at fiber-matrix interface investigated with molecular dynamics. *Composites Part B: Engineering*, 228: 109449, 2022. ISSN 1359-8368.

[15] J.R. Taylor. *Classical Mechanics*. G - Reference,Information and Interdisciplinary Subjects Series. University Science Books, 2005. ISBN 9781891389221.

[16] L.D. Landau, L.P. Pitaevskii, A.M. Kosevich, and E.M. Lifshitz. *Theory of Elasticity: Volume 7*. Number v. 7. Elsevier Science, 2012. ISBN 9780080570693.

[17] Heinrich Hertz. Ueber die berührung fester elastischer körper. 1882(92): 156–171, 1882.

[18] Edward Dintwa, Engelbert Tijskens, and Herman Ramon. On the accuracy of the hertz model to describe the normal contact of soft elastic spheres. *Granular Matter*, 10:209–221, 2008. URL `https://doi.org/10.1007/s10035-007-0078-7`.

[19] U. Hartmann. Magnetic force microscopy. *Annual Review of Materials Science*, 29(1):53–87, 1999.

[20] Manuel Nonnenmacher, MP o'Boyle, and H Kumar Wickramasinghe. Kelvin probe force microscopy. *Applied physics letters*, 58(25):2921–2923, 1991.

[21] Hans-Jürgen Butt, Brunero Cappella, and Michael Kappl. Force measurements with the atomic force microscope: Technique, interpretation and applications. *Surface science reports*, 59(1-6):1–152, 2005.

[22] Franz J. Giessibl. Afm's path to atomic resolution. *Materials Today*, 8(5): 32–41, 2005. ISSN 1369-7021.

[23] Tomas P. Corrales. *Local dynamics and bending mechanics of mesostructured materials*. PhD thesis, Mainz, 2013.

[24] Sylwia Babicz-Kiewlicz. *Analysis of Atomic Force Microscopy Surface Images by Means of Higher-harmonic Tip Vibrations Modes*. PhD thesis, 2015.

[25] Chih-Wen Yang, Ing-Shouh Hwang, Yen Fu Chen, Chia Seng Chang, and Din Ping Tsai. Imaging of soft matter with tapping-mode atomic force microscopy and non-contact-mode atomic force microscopy. *Nanotechnology*, 18(8):084009, jan 2007.

[26] Q. Zhong, D. Inniss, K. Kjoller, and V.B. Elings. Fractured polymer/silica fiber surface studied by tapping mode atomic force microscopy. *Surface Science Letters*, 290(1):L688–L692, 1993. ISSN 0167-2584.

[27] Jeffrey Hutter and John Bechhoefer. Calibration of atomic-force microscope tips. *Review of Scientific Instruments*, 64:1868 – 1873, 08 1993.

[28] Gleb V. Shevchenko, Nikita A. Glubokov, Anton V. Yupashevsky, and Anna S. Kazmina. Air flow sensor based on environmental sensor bme280. In *2020 21st International Conference of Young Specialists on Micro/Nanotechnologies and Electron Devices (EDM)*, pages 432–435, 2020.

[29] Matías Tagle, Francisca Rojas, Felipe Reyes, Yeanice Vásquez, Fredrik Hallgren, Jenny Lindén, Dimitar Kolev, Agot K Watne, and Pedro Oyola. Field performance of a low-cost sensor in the monitoring of particulate matter in santiago, chile. *Environmental Monitoring and Assessment*, 192(171), 2020.